**FACULTY
OF MATHEMATICS
AND PHYSICS**
Charles University

MASTER THESIS

Radek Novotný

Molecular simulations of organic-inorganic hybrid materials

Department of Chemical Physics and Optics

Supervisor of the master thesis: doc. RNDr. Miroslav Pospíšil, Ph.D.

Study programme: Biophysics and Chemical Physics

Study branch: Chemical Physics

Prague 2022

I declare that I carried out this master thesis independently, and only with the cited sources, literature and other professional sources. It has not been used to obtain another or the same degree.

I understand that my work relates to the rights and obligations under the Act No. 121/2000 Sb., the Copyright Act, as amended, in particular the fact that the Charles University has the right to conclude a license agreement on the use of this work as a school work pursuant to Section 60 subsection 1 of the Copyright Act.

In .... date ....
<div align="right">Author's signature</div>

Title: Molecular simulations of organic-inorganic hybrid materials

Author: Radek Novotný

Department: Department of Chemical Physics and Optics

Supervisor: doc. RNDr. Miroslav Pospíšil, Ph.D., Department of Chemical Physics and Optics

Abstract: Layered double hydroxides (LDH) are a promising material for use as a drug carrier thanks to their capacity for the intercalation of various anionic species, as well as their very low toxicity for the human body. Atorvastatin (ATS) is a drug used for blood cholesterol level lowering and cardiovascular disease prevention. Current methods of ATS delivery are quite ineffective, leading to the need for prescribing high ATS doses, which may cause discomfort to patients due to the drug's adverse side effects, most commonly including nausea, indigestion, joint pain or muscle pain. The intercalation of ATS into LDH could facilitate a controlled, targeted release of the drug into the patient's body, making a lower dose of drug more effective and thus alleviating the side effects of ATS. Molecular simulations utilising the COMPASS force field were used to assess three different models of ATS intercalated into Mg_2Al LDH with ATS concentrations of 61.99 %, 73.64 % and 70.64 %, corresponding to basal spacing of LDH layers of 3.751 nm, 3.808 nm and 3.823 nm, taken from X-ray diffraction experiments. Different starting orientations of ATS anions in the LDH interlayers were explored. The highest concentration of ATS appeared the most promising and lead to the most stable structure. Geometry optimisations and subsequent molecular dynamics simulations showed that the ATS anions interact with the LDH layers through hydrogen bonding between carboxyl groups of ATS and hydroxyl groups of LDH. This interaction was observed in nuclear magnetic resonance experiments as well, confirming the validity of the molecular simulations' results.

Keywords: atorvastatin, intercalation, layered double hydroxides, molecular simulations

Contents

Introduction

In this thesis, we are mainly focusing on the investigation of various concentrations of atorvastatin molecule intercalated into layered double hydroxides (LDH). We use the techniques of molecular simulations, molecular mechanics (MM) and molecular dynamics (MD), (i) to determine the possible optimal spatial orientation and position of the atorvastatin molecules between the LDH layers, (ii) to compare our results with experimental measurements, including solid-state nuclear magnetic resonance (SSNMR) and powder X-ray diffraction (PXRD) and (iii) to determine the most probable and preferred concentration of atorvastatin molecules per LDH unit cell.

Atorvastatin was the most commonly prescribed drug in the United States in both 2018 and 2019 and it has been one of the top five most commonly prescribed drugs since 2014 (Kane, 2021). It is used to lower abnormally high levels of lipids in the patients' bloodstream as well as prevention against cardiovascular diseases (Drugs.com, 2022). However, as with most drugs, atorvastatin usage may experience side effects, which include joint pain, diarrhoea, nausea, and muscle pains, in some cases even rhabdomyolysis (rapid breakdown of skeletal muscles), diabetes or impeded liver function (Macedo et al., 2014; Ward et al., 2019). Studies have also been carried out, testing atorvastatin's toxicity to aquatic flora, and although atorvastatin itself does not appear to be toxic in the low concentrations which were detected in natural water, the photoproducts released from atorvastatin after being exposed to near-UV light did have a detrimental effect on studied aquatic plants (Klementová et al., 2021).

The obvious way of limiting the side effects mentioned above is lowering the dosage of the given medicine. To achieve that without diminishing the desired effects of the drug, the form of delivery needs to be modified and improved in such a way that allows the drug to act only in the desired way. A promising method of targeted delivery of the atorvastatin drug into the body and lowering its dosage is one application of LDH. It is achieved by intercalation of atorvastatin anions between layers of LDH. An advantage is that the continual release of atorvastatin is slowed down and, moreover, can be controlled (Shokrolahi et al., 2021).

Layered double hydroxides, also known as anionic clays, are a group of materials that consist of positively charged metal hydroxide layers alternating with anionic interlayers. While the hydroxide layers are quite robust and stable, the anionic species in the interlayers can be quite easily replaced with other anions, which is one of the most appealing features of LDH (Rives, 2001). The easiness of anionic exchange together with LDH's non-toxicity for the human body (up

to known amounts) (Cunha et al., 2016) makes them perfect for our investigated application of atorvastatin for oral route prescription. By intercalating an atorvastatin anion into LDH, we should be able to receive an intercalated material with more controlled and better targeted delivery, potentially allowing for lowering of the dosage and thus reducing the harmful side effects on the human body.

Apart from their use for drug delivery in pharmaceutics, LDH are also used in a wide range of other industrial and environmental applications, including as additives to polymers, in agriculture (Ureña-Amate et al., 2011), for adsorption of organic wastes (Chuang et al., 2008; Kameda et al., 2009), as catalysts, or in photo- and electrochemistry (Zong and Wang, 2014; Chen et al., 2010).

When working with a small system like a drug intercalated into LDH, experimental methods might not be able to provide all the information about the particular arrangement of molecules. That is why computational methods are very popular and useful when describing any molecular system. The main advantage of molecular simulations is helping us to determine the molecular arrangement of interlayer species and provide us with a description of mutual interactions (both bonding and non-bonding) within the structure. They help us better understand the LDH structure and enable us to evaluate the effect of different conditions on the LDH interlayer stability and structure and various boundary conditions, including the knowledge of all investigated interactions and energies characterising the calculated structure.

The main targets of this thesis are to use the techniques of molecular simulations to better understand the properties of various concentrations of atorvastatin intercalated into an LDH structure. Starting with parameters acquired from PXRD measurements, several variations of the atorvastatin-LDH system with different amounts and various orientations of the atorvastatin anions were prepared. By doing this, we hoped to gain a better insight into how the atorvastatin anions tend to arrange within the LDH and how they interact with the hydroxide layers. The software Materials Studio (Accelrys, 2004) was used to perform all the calculations and simulations. To verify calculated observations, experimental results of SSNMR were used.

1. Atorvastatin

Atorvastatin (ATS), or $C_{33}H_{35}FN_2O_5$, is an organic molecule consisting of a central pyrrole ring with a different group attached to each of the five atoms. Starting from the nitrogen, these groups are: a hexyl group with a carboxyl group at the end and hydroxyl groups on the third and fifth carbon; a 4-fluorophenyl group; a phenyl group; a phenyl group connected to the central carbon through a CONH group (a peptide bond); and an isopropyl group. A graphical representation of the molecule is shown in Figure 1.1.

Atorvastatin belongs to the category of statins, which are a class of medication used for their lipid-lowering properties. They target the enzyme that cataly-
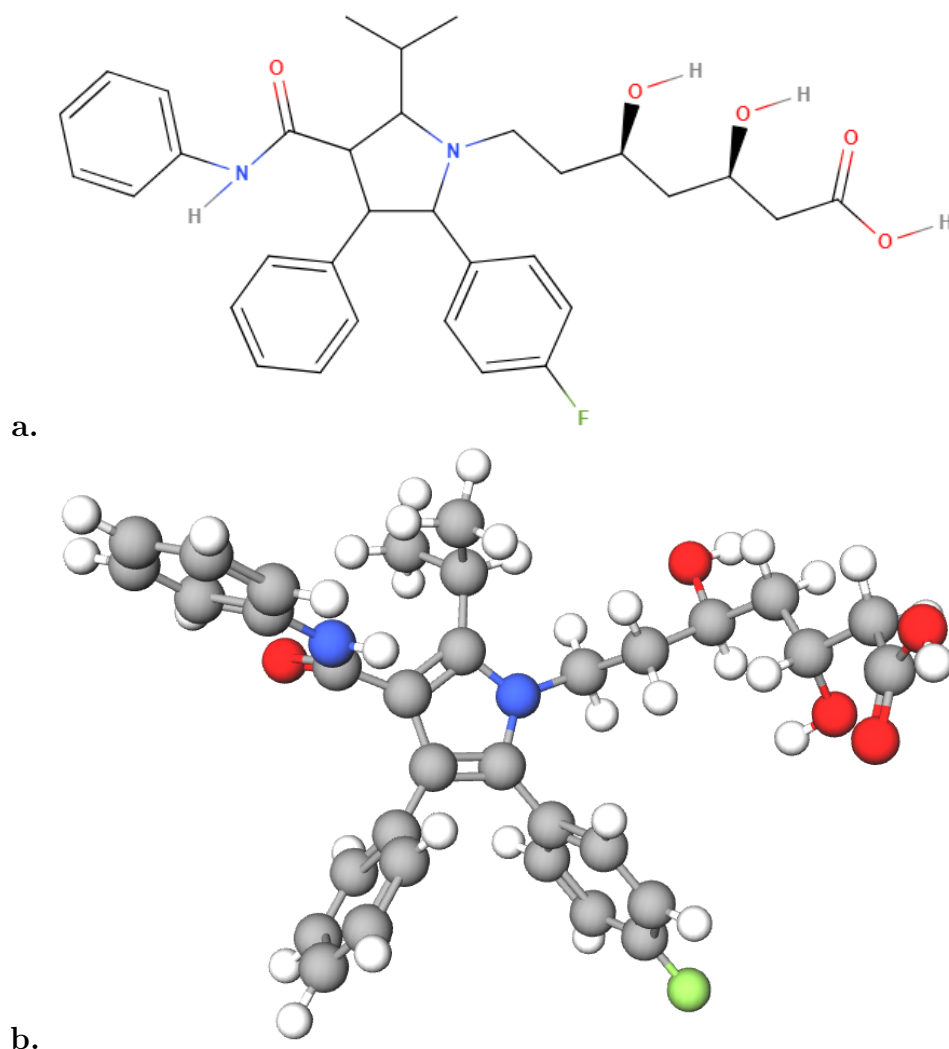

Figure 1.1: A molecule of atorvastatin: **a.** Schematic representation; **b.** 3-D representation using the ball-and-stick model, carbon atoms are shown in grey, hydrogen atoms in white, oxygen atoms in red, nitrogen atoms in blue and a fluorine atom in green (both created using `https://molview.org/`).

ses the conversion of 3-hydroxy-3-methylglutaryl co-enzyme A (HMG-CoA) into mevalonic acid, which is a crucial step in the biosynthesis of cholesterol. For this reason, statins are also known as HMG-CoA reductase inhibitors. According to the standard lipid hypothesis, the level of cholesterol in the individual's blood is closely linked to the likelihood of developing cardiovascular disease (Steinberg, 2004, 2006; Ference et al., 2017).

Atorvastatin is prescribed either to patients without coronary heart disease but with multiple risk factors as a preventive measure to reduce the risk of myocardial infarction, stroke or angina, or to patients with existing coronary heart disease in order to reduce the risk of myocardial infarction, stroke, congestive heart failure or angina (Grundy et al., 2019).

Currently, atorvastatin is available in the form of atorvastatin calcium salt. It is administered orally in the form of tablets and it is absorbed rapidly after administration. It has a very low bioavailability of around 14 % due to extensive first-pass metabolism meaning its concentration is greatly reduced before reaching the circulatory system (Karvaly et al., 2021).

1.1. Side effects

Adverse effects most commonly include joint pain, indigestion, diarrhoea, nausea, nasopharyngitis (inflammation of the pharynx and nasal cavities), insomnia, urinary tract infection and pain in extremities. Less commonly, patients report muscle aches or muscle weakness (Božina et al., 2021).

In some patients, for example, those with impaired renal function, rhabdomyolysis has been reported. Some data also suggest that statins may increase the risk of developing diabetes mellitus (Nemati et al., 2021).

There is no antidote for atorvastatin overdose. If patients suffer from adverse side effects, the only solution is reducing the dosage or halting treatment for some time. However, there might be an alternative solution in changing the form of administration in such a way that bioavailability would be increased so that the dosage may be decreased without losing the drug's effects. One class of materials that have been receiving attention as suitable for drug delivery systems are LDH (Kuthati et al., 2015).

2. Layered double hydroxides

LDH are sometimes referred to as hydrotalcites after one of the most common representatives, hydrotalcite, which was discovered in Sweden in 1842 (Rives, 2001) and was thoroughly studied as early as 1930 (Feitknecht and Gerber, 1942). LDH are a class of ionic solids which are characterised by their typical layered structure. Each layer consists of various metal cations between adjacent hydroxide layers on both sides. The interlayer consists of various anions and neutral molecules (most commonly water). These anions are only weakly bound to the metal hydroxide layers and are therefore often exchangeable with other anions, which makes LDH suitable materials for intercalation of various species.

Another, earlier used name for LDHs is anionic clays due to the anions intercalated between the metal hydroxide layers. This distinguishes them from cationic clays, a group of materials that are more commonly found in nature than anionic clays, which are frequently characterised by a layered structure composed from parallel tetrahedral and octahedral sheets, most commonly formed by silica and alumina (Bergaya and Lagaly, 2006).

2.1. Structure

Most LDHs can be represented by the following chemical formula:

$$[M^{2+}_{1-x}N^{3+}_x(OH^-)_2]^{x+}[(Z^{n-})_{x/n} \cdot yH_2O]^{x-}$$
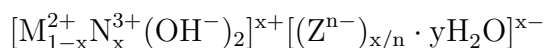
M and N are metal cations (element M can be different from N but also the same) and x is the ratio between them, which is usually between 0.2 and 0.4. Zn^- represents the intercalated anion (or anions), with n being the anion's charge and y being the number of water molecules. The reason why we do not observe x < 0.2 is likely due to too high main distance between the anionic layers, which results in a collapse of the structure. The upper limit of x $\approx$ 0.4 is generally contributed to electrostatic repulsion between the trivalent metal cations as well as the repulsion between the intercalated anions (Rives, 2001).

The most common naturally occurring anions include Cl^-, Br^-, NO_3^-, CO_3^{2-} or SO_4^{2-}. The metal hydroxide layer usually consists of two types of metal cations, divalent and trivalent. They can be cations of the same element or two different elements. The most common divalent cations are Mg^{2+}, Fe^{2+}, Co^{2+}, Ni^{2+}, Cu^{2+} and Zn^{2+} and the most common trivalent cations Al^{3+}, Cr^{3+}, Fe^{3+}, Co^{3+}, Ni^{3+} and Ga^{3+}. The reason why we do not see elements like Cd, Sc or La is that their ionic radii are too high (over 0.80 Å) and thus incompatible with forming

	Mg^{2+}	Fe^{2+}	Co^{2+}	Ni^{2+}	Cu^{2+}	Zn^{2+}	Ca^{2+}	Li^+
Al^{3+}	•	•	•	•	•	•	•	•
Cr^{3+}			•	•	•	•	•	
Fe^{3+}	•	•	•		•	•	•	
Co^{3+}		•	•	•				
Ni^{3+}				•				
Ga^{3+}	•	•	•	•	•	•	•	
Ln^{3+}				•			•	
Ti^{4+}			•					

Table 2.1: Observed possible combinations of (mostly) divalent and trivalent metal cations in LDH.

brucite-like layers (tetrahedral $M^{2+}(OH)_2$ layers). The nature of ordering of the two types of metallic cations is hard to detect experimentally and was thought to be random (Rives, 2001; Vucelic, 1997) but in recent studies, a regular structure has been observed (Krivovichev et al., 2010), especially for values of x = 0.33 or 0.25 (Sideris et al., 2008). The ordering might be caused by the trivalent cations' tendency to avoid close contacts and it might be possible that it is only a local ordering which does not fully hold for a longer range (Pimentel et al., 2022) which would explain why some studies reported random ordering (Zhitova et al., 2010). Apart from these most typical divalent-trivalent combinations, monovalent-trivalent (Li^+-Al^{3+}) or divalent-tetravalent (Co^{2+}-Ti^{4+}) arrangements are also possible as well as structures with more than two types of cations which have still not been properly investigated. Table 2.1, adapted from (de Roy et al., 1992), shows the possible combinations of divalent and trivalent (as well as monovalent Li^+ and tetravalent Ti^{4+}) metal cations that have been reported.

A model of a typical LDH structure is shown in Figure 2.1. The metal hydroxide brucite-like layers are composed of octahedral $M(OH)_6$ units with shared oxygen edges and a metal cation in the middle. These octahedra are however not quite regular as they would be in brucite; instead, they are flattened along the stacking direction, which lowers the symmetry from O_h (octahedral) to D_{3d} (dihedral, same symmetry as a triangular antiprism). The degree of flattening is dependent on the mean metal ionic radius of the cations and the larger this radius, the lower the thickness of the metal hydroxide layer and the larger the distance between the cations as well as between the OH^- groups (those that are on the same side of the layer) (Rives, 2001).
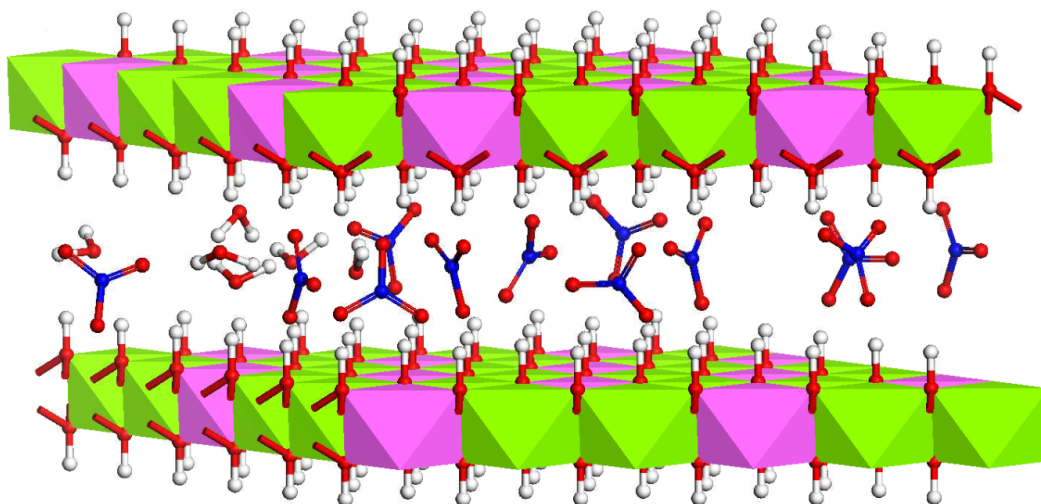
Figure 2.1: A typical LDH structure, in this case Mg$_2$Al LDH, with nitrate anions and water molecules in the interlayer. Metal cations in the hydroxide layers are represented by colourful tetrahedra – magnesium in green and aluminium in light blue. The rest of the atoms are represented by the ball-and-stick model – hydrogen in white, oxygen in red, nitrogen in blue (figure created in Materials Studio (Accelrys, 2004).

The anion interlayer is much less rigid compared to the metal hydroxide layer. In fact, it is not a crystalline structure at all but a collection of separate anions, which are usually connected to each other and to the hydroxide layer only by weak non-bond interactions, such as hydrogen bonding or electrostatic and van der Waals interactions. As such arrangement can be quite flexible, the basal spacing between the metal hydroxide layers depends not only on the kinds of intercalated anions but sometimes on their specific arrangement as well (Mishra et al., 2018). Finally, the interlayer contains water molecules which interact with the anions and the hydroxide layers to create coordinated spheres.

Apart from the naturally occurring inorganic anions mentioned earlier, the LDH structure can host a plethora of various anionic species, including different anionic complexes, organic anions such as carboxylates, phosphonates, alkyl sulphates, benzoates and others, or even biomolecules such as DNA, amino acids, vitamins, peptides, nucleosides etc. (Mishra et al., 2018).

The intercalated anions tend to arrange themselves in a way which maximises the interaction with the hydroxide layers. For small inorganic anions, this usually means simply lying parallel to the layers, close to the hydroxyl groups. Larger organic molecules tend to interact with the hydroxide layers through hydrogen bonding to the hydroxyls so they arrange themselves with their anionic groups (e. g., COO$^-$) facing the hydroxide layers while the hydrophobic ends of the molecule stay in the middle of the interlayer, away from the hydroxyl groups (Fernon et al., 1994).

2.2.   Preparation methods

Several different ways to synthesise LDHs have been reported. The choice of method is usually connected with the intended application of the LDH.

Co-precipitation

The most common method of preparation of intercalated LDH is co-precipitation. It works by slow addition of a mixed solution of divalent and trivalent metal salts into a reactor containing water. The pH needs to be kept at a specific value for the co-precipitation of the two metal salts to occur and so an alkaline solution is added as well. The metal hydroxide brucite-like layers are formed through the condensation of hexa-aquo complexes in the solution. The intercalated anions can come either from the initial mixing salts or from the added alkaline solution (if the pH) is very high. Alternatively, the anions that are meant to be intercalated can already be present as a solution in the reactor before the start of the co-precipitation. The controlled experimental conditions in the reactor determine which of the anions mentioned above are intercalated.

The pH in the reactor during the co-precipitation also has a large influence on the process. Most types of LDH structures only form if the pH is kept in a specific range. For example, when preparing a Zn_2Al-LDH with intercalated Cl^- anions, a well-ordered hydrotalcite-like structure forms if prepared at pH ranging from 7.0 to 10.0. However, at lower than 7.0 pH values, an amorphous compound is obtained, whereas at pH higher than 10.0, brucite-type $Zn(OH)_2$ forms alongside the hydrotalcite-like LDH (Rives, 2001).

Anionic exchange

Anionic exchange is simply the exchange of anions present in the interlayers of an LDH (which was usually prepared by co-precipitation) for a different anion. This is usually performed by stirring the precursor LDH in a solution which contains an excess of the anion that is to be intercalated. The whole process is most commonly carried out under an inert atmosphere in order to avoid contamination by carbonates. The rate of exchange generally depends on the electrostatic forces between the LDH host and the anions that are being intercalated (Morel-Desrosiers et al., 2003).

Reconstruction

This is an interesting method as it utilises the memory effect present in some LDHs (Chibwe and Jones, 1989). The LDH is mildly calcinated (heated to a

temperature around 400–500 °C) in an inert atmosphere which removes the original intercalated anions as well as any water molecules and transforms the cationic hydroxide layers into the respective metal oxides. These oxides are then immersed in an aqueous solution of the anionic species that are to be intercalated. The exposure to water causes the oxides to revert back to the LDH structure, now with the desired anions intercalated between the layers (Rives et al., 2014).

Other methods

Other methods of LDH preparation exist but are generally less common than co-precipitation. For example, induced hydrolysis is a method consisting of two steps. First, a trivalent metal oxide is precipitated by an alkaline solution. Then, the resulting precipitate is slowly added to a solution of a divalent metal salt at a constant pH, which induces a controlled release of the trivalent metal and an LDH phase is formed (Rives, 2001).

2.3.   Properties

LDH have many interesting properties that can be used and harnessed in various ways. The first one is high specific surface area, which is total surface area per unit of mass, usually measured by adsorption of N_2 gas. The sample is put in a low-pressure cell, which is slowly filled with nitrogen until saturation is reached and no more gas adheres to the sample's surfaces. Then, the sample is heated to release the gas and the surface area is calculated from the dependence of the adsorbed gas volume on the pressure in the cell. Most often, the Brunauer-Emmett-Teller (BET) isotherm method (Brunauer et al., 1938) is used for the calculation. Thanks to the high surface area, LDH have good adsorption properties and are useable as catalysts for various chemical reactions. Another property useful for catalysts is the homogenous dispersion of metal ions throughout the layers. This dispersion of metals can also lead to unusual alkaline or hydrogenating properties depending on the composition. However, probably the most widely studied property is LDH's good capacity for anion exchange with respect to human health (Del Hoyo, 2007).

A unique and advantageous property of LDHs is the fact that the hydroxide layers are positively charged and the interlayers, therefore, need to be negatively charged. This differentiates LDHs from other types of clays where the interlayers are charged positively and makes them perfect for the intercalation of various anions (Bergaya and Lagaly, 2006).

2.4.   Applications

Thanks to the compositional variation in both the hydroxide layers and the anionic interlayers, LDHs can be used in a variety of applications, including wastewater treatment, ion exchange, flame retardation, as an antacid (neutralisation of stomach acids), polymer stabilisation, as a catalyst or catalyst precursor, in agriculture or for pharmaceutical use (Mishra et al., 2018; Rives et al., 2013, 2014).

Due to their surface chemical properties and their versatile chemical composition, LDH are an attractive material for use in ceramics. Specifically, LDH of different chemical compositions can produce different colours which are used as pigments. For example, by step-wise heating of Ni-Al LDH, one can obtain cyan or pale-blue nano-pigments useable for ceramics (Gabrovska et al., 2015) and Co-Al LDH prepared by co-precipitation can produce pink colour (Arai and Ogawa, 2009).

As mentioned above, LDH have a very high surface area per unit of mass and large porosity which makes them ideal materials for use as adsorbents. They can remove toxic metals and ions from water (Yang et al., 2014) and air (Chuang et al., 2008) through adsorption. Removal of organic compounds from water using the adsorption properties of LDH has also been demonstrated (Chuang et al., 2008; Kameda et al., 2009; Chen et al., 2009). The adsorption properties combined with the ability to intercalate species into the LDH interlayer have led to the development of a lysozyme-LDH-based disinfectant. Lysozyme is an enzyme which has long been used as a disinfectant due to its ability to break down bacterial cell walls. After intercalating lysozyme into LDH, the resulting lysozyme-LDH disinfectant has a higher antibacterial activity than lysozyme on its own as the antibacterial activity of lysozyme is accompanied by the adsorption capabilities of LDH (Yang et al., 2013). Another advantage of lysozyme-LDH is that it does not produce any by-products which can be a problem with some other disinfectants (Watson et al., 2012).

The adsorption properties of LDH, as well as their capacity for intercalation have been utilised in agriculture as well. Not only can LDH be used to adsorb excess pesticides and herbicides from contaminated soil and water, but they can even be used as hosts for pesticides and herbicides, releasing them into the soil slowly and in a controlled manner thus avoiding harmful contamination of soil and groundwater altogether (Ureña-Amate et al., 2011).

LDH's capacity for intercalation can be utilised for the immobilisation of various species. By immobilisation is meant the imprisonment of particular species at a particular place. This process has many applications, including industrial production of amino acids, beverages or antibiotics, in the case of enzymes, it is

used in the production of jams, jellies and syrups or in the diagnosis and treatment of diseases or in research applications (Mishra et al., 2018). Immobilisation of nucleic acids is possible (Ladewig et al., 2010), as well as the immobilisation of bacteria and viruses (Jin et al., 2007). Enzymes immobilised in LDH can be used in biosensors, for example, urease used in urea (the main nitrogen-containing substance in the urine of mammals) biosensors for medical diagnostics and monitoring (Barhoumi et al., 2006).

If an antimicrobial species is intercalated into LDH, the resulting material has antimicrobial properties. For example, silver nano particles have been intercalated into Zn-Al LDH resulting in a material with antibacterial properties (Chen et al., 2011). Zn-Ti LDH nanosheets have been found to exhibit antimicrobial activity when illuminated by visible light, particularly strong against *Escherichia Coli* (bacteria found in the lower intestine, most strains are harmless, but some may cause food poisoning) (Zhao et al., 2013).

LDH have many prospective applications in the biomedical field. Thanks to their low toxicity and advanced biocompatibility, LDH are ideal for drug delivery (Kura et al., 2014). Many different drugs have been successfully intercalated into LDH, including anti-inflammatory drugs (Rives et al., 2013), antidiabetics, antibiotics, antioxidants, cardiovascular drugs, amino acids and peptides (Rives et al., 2014). The main reason to use LDH for drug delivery is the facilitation of controlled, sustained release of the drug into the human body (Mishra et al., 2017). Apart from that, intercalation into LDH can decrease the toxicity of a drug (Bullo et al., 2013) and enhance the effects of anti-cancer drugs (Sugano et al., 2010). The cholesterol-lowering drug atorvastatin can also be intercalated into LDH (Shokrolahi et al., 2021) which should help control its release and improve bioavailability.

3. Molecular simulations

Experimental methods, which are used to describe LDH as well as other crystalline materials, have their limitations. To get a more detailed insight into the atomic structure of these and other disordered materials, various computational and modelling techniques are employed. Ab initio quantum mechanical calculations are, of course, the most detailed and most precise. However, even with today's computational capacities, they can still be applied only to relatively small systems (if we want the calculations to finish in a reasonable amount of time). Therefore, for larger systems, such as LDH, less computationally demanding methods need to be considered.

One widely used method is the empirical force field (FF) approach which calculates the potential energy of a system by evaluating forces between all atoms in the system. The basis for these forces is classical mechanics, no quantum mechanical effects are taken into account, atoms basically behave as charged balls oscillating on springs and electrons immediately occupy their relaxed states in the atoms. This puts some limitations on the information we can harness from a molecular simulation calculation, but it is still a very useful tool for structure analysis. From the attained potential energy and its first and second derivatives, we gain information sufficient for performing a structural optimisation (i. e. finding an arrangement of atoms of the system with the lowest energy), performing a vibrational analysis and dynamics simulations (Comba et al., 2009).

3.1. Force fields

Force fields are made up of energy terms representing different interactions (Ermer, 1976). There are so-called valence (or through-bond) terms, which describe mainly the bonds between atoms and depend on geometrical properties like bond length, bond angle, torsion or inversion, as well as short-range non-bond interactions described by the Urey-Bradley potential, and through-space terms that depend on the interatomic distance, describing interactions like electrostatic attraction and repulsion, van der Waals interactions and hydrogen bonds. Together, these terms make up the expression for potential energy. We often break up this total energy E into its through-bond part E_d and through-space part E_{nd} (Comba et al., 2009).

$$E = E_d + E_{nd} \tag{3.1}$$

3.1.1. Through-bond interactions

We can break down the through-bond energy E_d into several terms, each describing a different characteristic of the bond between two atoms.

$$E_d = E_b + E_\theta + E_\phi + E_\delta \tag{3.2}$$

The first term E_b describes bond length deformation. We can employ the classic quadratic approximation assuming the bonded atoms behave as harmonic oscillators guided by a potential in the shape of a parabola, with a positive bonding constant k_b; r_{ij} being the instantaneous distance between atoms i and j and r_0 being the equilibrium distance between them.

$$E_b = \frac{1}{2}k_b\left(r_{ij} - r_0\right)^2 \tag{3.3}$$

A real bond does not behave strictly harmonically and we can improve upon this formula either by adding more terms (e. g., cubic and so on) or by replacing the harmonic potential with the Morse potential, resulting in bonding energy E_{bM}. The constant D_0 denotes the well depth.

$$E_{bM} = D_0\left[1 - \exp\left(-\sqrt{\frac{k_b}{2D_0}}\left(r_{ij} - r_0\right)\right)\right]^2 \tag{3.4}$$

The next term E_θ characterises valence bond deformation and is constructed analogously to the bond length term as a harmonic oscillator with a constant k_θ.

$$E_\theta = \frac{1}{2}k_\theta\left(\theta_{ijk} - \theta_0\right)^2 \tag{3.5}$$

Different variations of this term exist; some force fields use cosine functions instead of simply the angle values (Mayo et al., 1990), others use Fourier terms (Allured et al., 1991) or a harmonic sine function (Comba et al., 1995). Besides the force coming from the deformation of the angle, some force fields describe the direct interaction between the atoms i and k (the two atoms that are not connected by a bond but are both bonded to the same atom), often using the Urey-Bradley potential (Urey and Bradley, 1931). It contains two constants k_{UB0} and k_{UB1} and looks a little similar to the bond potential E_b, so we can think of it as describing an imaginary bond between the atoms i and k.

$$E_{UB} = \frac{1}{2}k_{UB0}\left(r_{ik} - r_0\right)^2 + k_{UB1}\left(r_{ik} - r_0\right) \tag{3.6}$$

The term E_ϕ is used to characterise the torsional deformations around a bond. The most commonly used potential contains a constant k_ϕ describing the potential barrier that needs to be overcome and is periodic with multiplicity m.
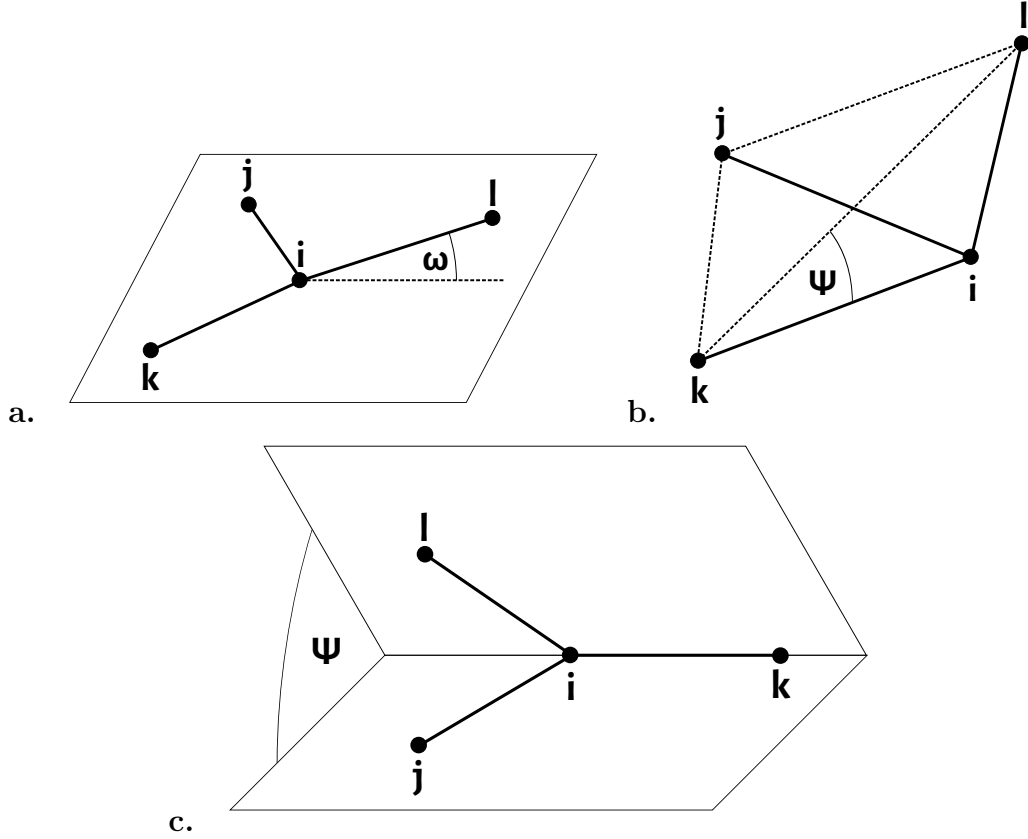
15

Figure 3.1: The three different types of inversions: **a.** Umbrella inversion; **b.** CHARMm inversion; **c.** AMBER inversion.

$$E_\phi = \frac{1}{2} k_\phi \left[1 + \cos \left(m \left(\phi_{ijkl} - \phi_0 \right) \right) \right] \tag{3.7}$$

The last term E_δ pertains to the out of plane deformation of a mutually bonded group of 4 atoms and one of them is out of plane. Examples of three different ways of description are shown in Figure 3.1.

Umbrella inversion $E_\delta = \frac{1}{2} k_\omega \left(\cos \omega - \cos \omega_0 \right)^2$

CHARMm inversion $E_\delta = \frac{1}{2} k_\Psi \left(\Psi - \Psi_0 \right)^2$

AMBER inversion $E_\delta = \frac{1}{2} k_\Psi \cos \left[n \left(\Psi - \Psi_0 \right) \right]$

3.1.2. Through-space interactions

The interactions contained in the term E_{nd} are not dependent on the existence of a bond between atoms and propagate directly through space. They are energies of electrostatic interactions E_ε, van der Waals interactions E_{vdW}, and hydrogen bonding E_{Hb}.

$$E_{nd} = E_\varepsilon + E_{vdW} + E_{Hb} \tag{3.8}$$

The electrostatic interactions are most often described using the charges q_i and q_j at each atom, the interatomic distance d_{ij} and permittivity constant ε.

$$E_\varepsilon = \frac{1}{\varepsilon} \frac{q_i q_j}{d_{ij}} \qquad (3.9)$$

Some force fields also include another term describing electronic polarisation (Mackerell, 2004) and others describe electrostatic interactions through dipole-dipole interactions.

Several different interactions of permanent electric dipoles and multipoles are all contained in the van der Waals term E_{vdW}. There are different potentials that can be used. All of them use a $1/r^6$ term for the attractive forces but they differ in the way they represent the repulsive part of the interaction. The momentary distance between the two atoms i and j is denoted d_{ij} and d_{ij}^0 stands for the distance at equilibrium. The letters A, B, C, D, F and G are constants.

Lennard-Jones potential: $E_{vdW} = \frac{A}{d_{ij}^{12}} - \frac{C}{d_{ij}^6}$ (Jones, 1924).

Buckingham potential: $E_{vdW} = A\exp(-Bd_{ij}) - \frac{C}{d_{ij}^6}$ (Buckingham, 1938).

Hill potential: $E_{vdW} = k_{vdW}\left(2.9 \cdot 10^5 \exp\left(-12.5\frac{d_{ij}}{d_{ij}^0}\right) - 2.25\left(\frac{d_{ij}^0}{d_{ij}}\right)^6\right)$.

Hydrogen bonding interactions E_{Hb} are sometimes included in the van der Waals and electrostatic interactions, but most often, they are represented by a potential similar to the Lennard-Jones potentia (Comba et al., 2009).

$$E_{Hb} = \frac{F}{d_{ij}^{12}} - \frac{G}{d_{ij}^{10}} \qquad (3.10)$$

Angular terms can sometimes be included in the hydrogen-bonding potential by adding terms with cosine functions (Comba et al., 1995). As we can see by comparing the exponents in the functions, the van der Waals interactions E_{vdW} and the hydrogen bonding interactions E_{Hb} are much less far-reaching compared to the electrostatic interactions E_ε as the higher exponents in the denominator decrease much quicker with increasing distance.

All the interactions get significantly weaker with increasing interatomic distance, yet the used potential never goes to zero. This means that if we were to use them in calculations as they are, we would need to calculate interactions between every two individual atoms which is not only necessary as the interactions are negligible over longer distances but also exceedingly computationally demanding, and it would make the calculations scalable only with great difficulty. For this reason, it is common practice to truncate the potentials at a certain distance from the interacting atom (Brooks et al., 1985). To avoid discontinuities in energy, the truncation is often done by continuously leading the potential to zero at some distance using a quadratic polynomial function. So that dipoles are not acciden-

tally split with this cut-off, charge groups are often created in which atoms are always counted together and cannot be separated by cut-off distance.

One commonly used method, which is very effective for periodic systems, is Ewald summation (Wells and Chaffee, 2015). In this method, the lattice sum S_m, used to express the interaction potential, is broken up into two parts, a short-range part and a long-range part, using a convergence function $\phi(r)$ which converges quickly to zero with increasing r.

$$S_m = \frac{1}{2} \sum_{L,i,j} \frac{A_{ij}}{|r_i - r_j - R_L|^m} = \tag{3.11}$$

$$= \frac{1}{2} \sum_{L,i,j} \frac{A_{ij}\phi_m\left(|r_i - r_j - R_L|\right)}{|r_i - r_j - R_L|^m} + \frac{1}{2} \sum_{L,i,j} \frac{A_{ij}\left(1 - \phi_m\left(|r_i - r_j - R_L|\right)\right)}{|r_i - r_j - R_L|^m} \tag{3.12}$$

The first sum quickly converges. If we use Fourier transformation on the second sum, we transform it into a sum in the reciprocal space and it then converges quickly as well.

3.1.3. Parametrisation and force field types

The general formulas listed above contain constants (or parameters), the values of which need to be determined and included in the force field when the force field parameters are created. These parameters are usually obtained empirically from experimental data. Generally, we recognise two types of force fields: first-generation force fields use parameters gained mainly from experimental measurements and second-generation force fields are initially based on ab initio calculations with subsequent use of empirical data for minor corrections and refinement of parameters (González, 2011).

As different materials may behave differently, a force field that was parametrised using a certain type of material should usually only be used on the same or similar materials. Thus, we receive different force fields, for example, Consistent Valence Force Field (CVFF) (Dauber-Osguthorpe et al., 1988) which can be used for small crystals, peptides, amino acids or gaseous structures; Assistant Model Building with Energy Refinement (AMBER) force field (Cornell et al., 1995) which is a family of force fields used mainly for proteins and nucleic acids, the Dreiding force field (Mayo et al., 1990) which is a general force field useful for most organic and inorganic molecules (but not crystals).

The Condensed-phase Optimized Molecular Potentials for Atomistic Simulation Studies (COMPASS) force field (Sun, 1998), which was used in this thesis, is a general force field based on ab initio calculations combined with experimental

data. It was parametrised against a large number of experimental observations for organic compounds and was validated using condensed phase properties as well as data for molecules in isolation. It is suitable for most solid materials and provides good agreement with experiments, which is useful for molecular dynamics.

Another example of a widely used force field is the so-called Universal Force Field (UFF) (Rappe et al., 1992) which is based on the general properties of elements and describes all the elements in the periodic table. It is one of the most general force fields which comes at a price of being less precise.

3.1.4. Charge equilibration

The charge equilibration method (QEq) is used for calculating the distribution of charge within a molecule (Rappe and Goddard, 1991). It's based on expressing the energy of an isolated atom E_A as a function of its charge Q_A. A Taylor expansion of the energy is then performed.

$$E_A\left(Q_A\right) = E_{A0} + Q_A\left(\frac{\partial E}{\partial Q}\right)_{A0} + \frac{1}{2}Q_A^2\left(\frac{\partial^2 E}{\partial Q^2}\right)_{A0} + \ldots \tag{3.13}$$

The energy of a neutral atom is E_{A0}. For atoms with charges -1 and +1 we get the following equations.

$$E_A\left(-1\right) = E_{A0} - \left(\frac{\partial E}{\partial Q}\right)_{A0} + \frac{1}{2}\left(\frac{\partial^2 E}{\partial Q^2}\right)_{A0} \tag{3.14}$$

$$E_A\left(+1\right) = E_{A0} + \left(\frac{\partial E}{\partial Q}\right)_{A0} + \frac{1}{2}\left(\frac{\partial^2 E}{\partial Q^2}\right)_{A0} \tag{3.15}$$

We can add and subtract these equations to get the expressions for electronegativity χ_A^0 of an atom and Coulombic repulsion J_{AA}^0 between two electrons in the atom's orbital. We define ionisation energy $I_A = E_A\left(+1\right) - E_{A0}$ as the energy needed to separate an electron from a neutral atom and electron affinity $E_A = E_{A0} - E_A\left(-1\right)$ as energy released when a neutral atom gains an electron.

$$\left(\frac{\partial E}{\partial Q}\right)_{A0} = \frac{1}{2}\left(I_A + E_A\right) = \chi_A^0 \tag{3.16}$$

$$\left(\frac{\partial^2 E}{\partial Q^2}\right)_{A0} = I_A - E_A = J_{AA}^0 \tag{3.17}$$

From this, we get a new expression for the energy of an isolated atom.

19

$$E_A\left(Q_A\right) = E_{A0} + Q_A\chi_A^0 + \frac{1}{2}Q_A^2 J_{AA}^0 \tag{3.18}$$

The total charge is then calculated by addition over all atoms. If the charge distributions of two atoms overlap, we need to correct for this by taking into account shielding.

To receive the chemical potential of an atom χ_A, we perform derivation with respect to the charge Q_A. To achieve equilibration, the chemical potentials of all atoms in the system must be equal.

$$\chi_1 = \chi_2 = \cdots = \chi_N \tag{3.19}$$

At the same time, the sum of charges on each atom must be equal to the overall charge of the molecule. From these two conditions, we receive N equations which are then solved for the N charge values on each atom.

3.2. Molecular mechanics

Molecular mechanics focus on the static (conformational) properties of materials. We are looking at the shape of the potential energy surface from which the geometrical arrangement of the structure is determined as well as its first derivatives which give us nuclear vibrations.

3.2.1. Minimisation algorithms

The main task of molecular mechanics is to find the minimum of the investigated system's potential energy by repeatedly calculating the total energy of the system and then slightly changing the structure in an effort to achieve lower energy. These two steps are repeated in a process called minimisation or geometry optimisation until the last reorganisation of the structure brings a smaller improvement in energy than what was set as the convergence criterion at the beginning of the optimisation. As the system is made up of N atoms and each can move in 3 spatial directions, we are basically trying to find the minimum of potential energy by moving in a $3N$-dimensional space. Several algorithms are used to find this minimum, each employed under different conditions.

Steepest descent

This method, as the name suggests, looks for the minimum by navigating the $3N$-dimensional space by always moving in the direction of the steepest gradient of the energy function (Debye, 1909). The algorithm continues along this direction
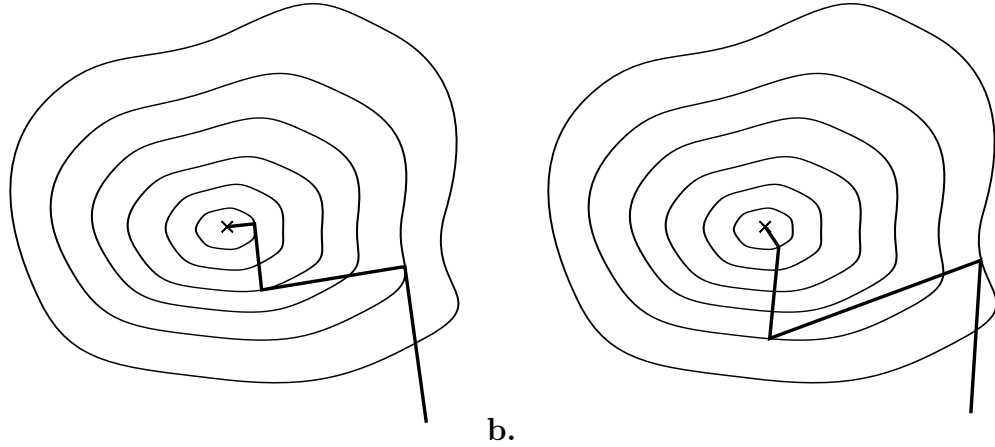
Figure 3.2: The steepest descent algorithm for finding a minimum: **a.** classic line search – the trajectory segments are perpendicular to each other; **b.** simplified line search – no longer perpendicular.

until it encounters a point at which the energy in this direction starts increasing again. That means the trajectory has touched the energy contour line and so the next steepest gradient direction is perpendicular to the previous one. The point at which this happens is found by moving along the line and checking the energy at two points close to each other until the minimum is 'trapped' between them. As is shown in Figure 3.2, the algorithm keeps 'zig-zagging' in two perpendicular directions until the convergence criteria are met. Such a method of finding the minimum along the line is called line search and can be quite slow as the energy needs to be calculated repeatedly for two different points during each step. An alternative to line search is simply choosing a random point along the direction of the steepest descent, and if the energy is lower than in the previous one, this point is chosen as the next starting point in which the steepest gradient is calculated (note that now, the new gradient direction will not be perpendicular to the previous one). This greatly reduces the number of times that energy needs to be calculated during one step.

We can easily imagine that with the steepest descent algorithm, the steps get increasingly shorter as we are approaching the minimum and so the calculation keeps slowing down. It is, therefore, useful to start our search with this algorithm and then, after we are close enough to the minimum, to switch to one of the following methods to save computation time.

Conjugate gradients

The conjugate gradient method is similar to the steepest descent method but the key difference is in the way that the new directions are selected (Hestenes and Stiefel, 1952). Each new direction h_{i+1} is chosen by modifying the previous

direction h_i with the gradient g_{i+1} at the point $i + 1$.

$$h_{i+1} = \gamma_i h_i + g_{i+1} \tag{3.20}$$

There are generally two possible ways of generating the constant γ_i. The Polak-Ribiere (Polak and Ribière, 1969) method:

$$\gamma_i = \frac{(g_{i+1} - g_i) \cdot g_{i+1}}{g_i \cdot g_i} \tag{3.21}$$

Or the Fletcher-Reeves (Fletcher, 1964) method:

$$\gamma_i = \frac{g_{i+1} \cdot g_{i+1}}{g_i \cdot g_i} \tag{3.22}$$

As this method needs to ensure the new gradient is conjugated to the previous one, we have to consistently find the minimum in the current direction in each step, speeding up the process by selecting a random point as in the steepest descent method is not possible. This means that the energy needs to be calculated several times in each step, and thus each the individual step takes longer than in the previous method. However, the conjugate gradient method converges to the energy minimum in fewer steps, so the overall speed is better.

It is important to note that this method works best when the energy function has a shape close to a quadratic function, meaning we need to be already quite close to the minimum. Therefore, the ideal approach is to use the steepest descent method for a few steps to get closer to the minimum and then switch to conjugate gradients to converge to the minimum faster. Parameters of optimisation can be set to determine the most advantageous moment for switching to the next method.

Both steepest descent and conjugate gradient methods scale linearly with the system's size as they only use the first derivative and are therefore suitable even for larger systems. The following method is more sophisticated and uses the second derivative as well, which means that the amount of memory and time needed scales with N^2.

Newton-Raphson method

The basic Newton-Raphson method tries to find the energy minimum r_{min} using the gradient $\nabla E(r_0)$ in combination with the Hessian (matrix of second derivatives) $\mathbf{A}(r_0)$ in the starting point r_0 (Accelrys, 2004).

$$r_{min} = r_0 - \mathbf{A}^{-1}(r_0) \cdot \nabla E(r_0) \tag{3.23}$$

This process is repeated until we satisfy the convergence criteria. As mentioned above, this method requires more time and memory than steepest descent

and conjugate gradients and scales quadratically with the size of the system and is, therefore, most suitable for smaller systems. Moreover, it requires the energy function to be even closer to a quadratic shape than in the case of the conjugate gradients method. This means that it should really only be used when we are fairly certain that we are close to the minimum, as if applied too far away from the minimum, it may become unstable. The advantage of this method is its great accuracy; it is used to finely refine the location of the minimum, for example, for the purpose of calculating vibrational frequencies the determination of which is very sensitive to even the smallest errors.

Variations of this method include the quasi-Newton (Broyden, 1972) method or the adjusted basis set Newton-Raphson, which are both available in Materials Studio.

3.2.2. Criteria of convergence

With all the minimisation methods, we decide that we have reached convergence when the difference in certain quantities at the current point and at the previous one gets below a certain pre-defined level. The most basic criterion of convergence is the difference in energy and difference in position. If we are using methods that calculate the second and first derivatives, we can use those as well, usually in the form of the sum of squares (Accelrys, 2004).

3.3. Molecular dynamics

The task of molecular dynamics is calculating forces that act on atoms in a system and then moving the atoms in reaction to these forces. To do this, classical Newtonian equations of motion need to be solved for every atom in the system. Being able to observe the dynamic progression of a system in time can be useful to us for several reasons. For example, it may help us to find possible lower-energy conformations of molecules of the system. Or we can study the movements of molecules during the system's evolution in time, find diffusion coefficients, and investigate other thermodynamic and structural properties of the system.

3.3.1. Integrational algorithms

At every step of a MD calculation, we need to solve the Newtonian equations of motion for every atom and find its position $\mathbf{r}_i$ and velocity $\mathbf{v}_i$. Therefore, we need an integrational algorithm that is quick and, at the same time, not too computationally demanding to find the position and velocity at time $t + \Delta t$ using only the position and velocity at time t.

$$\frac{\mathrm{d}V}{\mathrm{d}\mathbf{r}_i} = \frac{\mathrm{d}^2\mathbf{r}_i}{\mathrm{d}t^2} \qquad (3.24)$$

The most basic algorithm would be Euler's forward method which is a basic numerical method for solving differential equations. However, it is easy to see that this algorithm is not suitable for MD calculations as it is not time reversible and it violates Liouville's theorem as it does not preserve phase-space (Tuckerman, 2010).

Verlet algorithm

An example of a time reversible algorithm that preserves phase-time and does not require too much computer memory is the Verlet algorithm. We write position at time $t + \Delta t$ and at time $t - \Delta t$ in the following way.

$$\mathbf{r}_i\left(t + \Delta t\right) = \mathbf{r}_i\left(t\right) + \Delta t \mathbf{v}_i\left(t\right) + \frac{\Delta t^2}{2m_i}\mathbf{f}_i\left(t\right) + \frac{\Delta t^3}{3!}\dddot{\mathbf{r}}_i\left(t\right) + \mathcal{O}\left(\Delta t^4\right) \qquad (3.25)$$

$$\mathbf{r}_i\left(t - \Delta t\right) = \mathbf{r}_i\left(t\right) - \Delta t \mathbf{v}_i\left(t\right) + \frac{\Delta t^2}{2m_i}\mathbf{f}_i\left(t\right) - \frac{\Delta t^3}{3!}\dddot{\mathbf{r}}_i\left(t\right) + \mathcal{O}\left(\Delta t^4\right) \qquad (3.26)$$

From these equations, we can get the expressions for the position by adding them together and for velocity by subtracting them from each other.

$$\mathbf{r}_i\left(t + \Delta t\right) = 2\mathbf{r}_i\left(t\right) - \mathbf{r}_i\left(t - \Delta t\right) + \frac{\Delta t^2}{m_i}\mathbf{f}_i\left(t\right) + \mathcal{O}\left(\Delta t^4\right) \qquad (3.27)$$

$$\mathbf{v}_i\left(t\right) = \frac{\mathbf{r}_i\left(t + \Delta t\right) - \mathbf{r}_i\left(t - \Delta t\right)}{2\Delta t} + \mathcal{O}\left(\Delta t^3\right) \qquad (3.28)$$

As we can see, the velocity at time t is only available after the position at time $t + \Delta t$ has been calculated, so always one step later. This algorithm suffers from low precision because the value that is stored between steps is the position of atoms which is a big number that changes only a little, which means the accuracy of storage as a binary number is quite low. For initialisation, we need $\mathbf{r}_i\left(t - \Delta t\right)$, which can be approximated, for example, based on Taylor expansion (Schiller, 2005).

Verlet-leapfrog algorithm

An improvement of the Verlet algorithm is the Verlet-leapfrog algorithm which is probably the most commonly used in MD calculations. The name refers to the fact that the velocities are calculated at $t + \frac{\Delta t}{2}$, so they always 'leap' ahead of the positions.

$$\mathbf{r}_i \left(t + \Delta t \right) = \mathbf{r}_i \left(t \right) + \Delta t \mathbf{v}_i \left(t + \frac{\Delta t}{2} \right) \tag{3.29}$$

$$\mathbf{v}_i \left(t + \frac{\Delta t}{2} \right) = \mathbf{v}_i \left(t - \frac{\Delta t}{2} \right) \frac{\Delta t}{m_i} \mathbf{f}_i \left(t \right) \tag{3.30}$$

The current velocities at time t can be approximated.

$$\mathbf{v}_i \left(t \right) = \frac{\mathbf{v}_i \left(t - \frac{\Delta t}{2} \right) + \mathbf{v}_i \left(t + \frac{\Delta t}{2} \right)}{2} \tag{3.31}$$

This algorithm is algebraically equivalent to the Verlet algorithm: it is time reversible, however, it does not preserve phase-space volume.

Velocity-Verlet algorithm

Another variant of Verlet algorithm is the velocity-Verlet which provides better precision and some consider it the ideal algorithm for MD.

$$\mathbf{r}_i \left(t + \Delta t \right) = \mathbf{r}_i \left(t \right) + \Delta t \mathbf{v}_i \left(t \right) + \frac{\Delta t^2}{2m_i} \mathbf{f}_i \left(t \right) \tag{3.32}$$

$$\mathbf{v}_i \left(t + \Delta t \right) = \mathbf{v}_i \left(t \right) + \frac{\Delta t}{m_i} \left[\mathbf{f}_i \left(t \right) + \mathbf{f}_i \left(t + \Delta t \right) \right] \tag{3.33}$$

As we can see from the equations, this algorithm gives us positions, velocities and forces at the same time. It is time-reversible and preserves phase-space volume. This algorithm is also more precise than the previous two because it stores velocities between steps instead of positions. Velocities usually differ a lot between two steps, and therefore storing them in the computer as binary numbers is more precise than storing positions. However, in order to store these velocity values, the algorithm requires more memory than Verlet-leapfrog.

3.3.2. Statistical ensembles

The default state when solving equations of motion is that the number of particles N is constant together with the total energy E and the system's volume V. In statistical mechanics and thermodynamics, such a system is described by the microcanonical (NVE) ensemble. However, while these assumptions are convenient for theoretical calculations, in real-life experiments, it is often much more convenient (and easier) to keep other quantities constant, for example, the pressure P or temperature T. Table 3.1 shows the different possible statistical ensembles (note that the last ensemble – generalised ensemble – has no extensive

Statistical ensemble	Independent quantities	Dependent quantities
Microcanonical	NVE	μPT
Canonical	NVT	μPE
Isoenthalpic-isobaric	NPH	μVT
Isothermal-isobaric (Gibbs)	NPT	μVH
Grand-microcanonical	μVL	NPT
Grand-canonical	μVT	NPL
Grand-isothermal-isobaric	μPR	NVT
Generalised	μPT	NVR

Table 3.1: Types of statistical ensembles. Parameters: N – number of particles, V – system volume, E – total energy, μ – chemical potential, P – system pressure, T – system temperature, H – total enthalpy, L – Hill energy ($L = E - \mu N$), R – Ray enthalpy ($R = E + PV - \mu N$) (Hünenberger, 2005).

independent variable, which means its size is not specified and therefore it is not an actual physical ensemble; we include it in the table for completeness).

Apart from the basic microcanonical ensemble, the most commonly used ensembles in molecular dynamic calculations are probably the canonical (NVT) ensemble and the Gibbs (NPT) ensemble. Volume is easily controlled in both experiments and simulations by introducing physical constraints around the system. The number of particles is generally conserved in simulations by default. To control the temperature in simulations, a few different methods can be used, called thermostats. Similarly, the pressure is controlled by barostats.

3.3.3. Thermostats

Apart from simply matching the conditions of an experiment, a thermostat algorithm can also be useful for studying temperature dependent processes, enhancing the efficiency of a conformational search or simply to avoid energy drifts caused by the accumulation of numerical errors during a simulation.

The instantaneous temperature $\mathcal{T}$ of a system is most often defined using the instantaneous kinetic energy $\mathcal{K}$.

$$\mathcal{T} = \frac{2}{k_B N_{df}} \mathcal{K} \tag{3.34}$$

$$\mathcal{K} = \frac{1}{2} \sum_{i=1}^{N} m_i \dot{\mathbf{r}}_i^2 \tag{3.35}$$

This ensures that the average temperature $\langle \mathcal{T} \rangle$ is equal to the macroscopic temperature T. Constant k_B is the Boltzmann constant, m_i and $\dot{\mathbf{r}}_i$ have their usual meaning of mass and velocity of i-th particle. N_{df} denotes the number of internal degrees of freedom which depends on the number of particles N, number of geometrical constraints N_c and number of external degrees of freedom N_r.

$$N_{df} = 3N - N_c - N_r \qquad (3.36)$$

The number of internal degrees of freedom depends on the boundary conditions; if stochastic and frictional forces are applied, $N_r = 0$, for periodic boundary conditions, $N_r = 3$ and for vacuum boundary condition $N_r = 6$.

As the instantaneous temperature $\mathcal{T}$ depends on the atomic internal velocities, there needs to be some control over the rate of change of these velocities. It is introduced by using a modification of the Newton's equation called the Langevin equation (Lemons and Gythiel, 1997).

$$\ddot{\mathbf{r}}_i(t) = m_i^{-1}\mathbf{F}_i(t) - \gamma_i(t)\dot{\mathbf{r}}_i(t) + m_i^{-1}\mathbf{R}_i(t) \qquad (3.37)$$

Here, $\mathbf{R}_i$ is a stochastic force acting on the atoms and γ_i is an atomic friction coefficient. If the stochastic force is used, the coefficient γ_i is always positive, but some thermostats do not use the last term of the equation, in which case γ_i can have any value as it no longer represents actual physical friction. The same coefficient γ is then used for all atoms; negative γ means heat flows from the heat bath to the system and positive γ means it flows form the system into the heat bath.

At this point, it is important to note the distinction between two types of velocities that appear in the calculations. The velocities $\dot{\mathbf{r}}_i$ that we have used in the previous equations are so-called internal velocities and they are equal to the real atomic velocities $\dot{\mathbf{r}}_i^0$ only in the case of $N_r = 0$. For other values of N_r, a correction is required.

$$\dot{\mathbf{r}}_i = \begin{cases} \dot{\mathbf{r}}_i^0 & \text{if } N_r = 0 \\ \dot{\mathbf{r}}_i^0 - \dot{\mathbf{r}}_{CM}^0 & \text{if } N_r = 3 \\ \dot{\mathbf{r}}_i^0 - \dot{\mathbf{r}}_{CM}^0 - \mathbf{I}_{CM}^{-1}(\mathbf{r}^0)\,\mathbf{L}_{CM}^0 \times (\mathbf{r}_i^0 - \mathbf{r}_{CM}^0) & \text{if } N_r = 6 \end{cases} \qquad (3.38)$$

$\mathbf{r}_{CM}^0$ are the coordinates of the system's centre of mass (CM), $\mathbf{L}_{CM}^0$ is the system's angular momentum around the CM and $\mathbf{I}_{CM}$ is the inertia tensor of the system relative to the CM. While the internal velocities $\dot{\mathbf{r}}_i$ are used in the Langevin equations, the atomic velocities $\dot{\mathbf{r}}_i^0$ are used to propagate the atomic coordinates simultaneously in time. Disregarding the distinction between the two

types of coordinates leads to the loss of linear and angular momenta conservation (Hünenberger, 2005).

Another important note concerns the propagation of heat in a system. In real-life thermostats, heat gradually diffuses from the system's surface to its centre and vice-versa, leading to inhomogeneities in temperature. However, in simulations, the velocities of all atoms are modified at the same time, which means the temperature changes simultaneously throughout the system. Thermostats which aim for more precision therefore employ simulated temperature fluctuations.

The Langevin equation, whether in its full or simplified form, is the basis for most temperature control algorithms. The following paragraphs provide a brief overview of the algorithms used.

Monte Carlo

The simplest way to generate a thermodynamical ensemble is the Monte Carlo (MC) algorithm. It does not include atomic velocities or kinetic energy; the moves of atoms are randomly generated and accepted with the following probability.

$$p = \min\left\{\exp\left(-\frac{\Delta\mathcal{U}}{k_B T}\right), 1\right\} \tag{3.39}$$

The probability p of accepting a move depends on the change in potential energy $\Delta\mathcal{U}$ associated with it. At constant volume V, the MC algorithm generates a canonical ensemble. It is non-smooth, non-deterministic, time-irreversible and does not provide any dynamical information about the system (Hünenberger, 2005).

Stochastic dynamics

The stochastic dynamics (SD) algorithm works by integrating the full Langevin equation. The stochastic forces $\mathbf{R}_i(t)$ have the following properties: (i) they are uncorrelated with the velocities $\dot{\mathbf{r}}_i(t')$ and systematic forces $\mathbf{F}_i(t')$ at time $t' < t$; (ii) force components $R_{i\mu}(t)$ are uncorrelated with any component $R_{j\nu}(t')$ along a different axis unless $i = j$, $\mu = \nu$ and $t' = t$; (iii) they average to zero over time and (iv) their mean square components are equal to $2m_i\gamma_i k_B T_0$.

The Langevin equation of motion is smooth, non-deterministic and time-irreversible. A trajectory generated by integrating the equation at constant volume V generates a canonical ensemble of microstates at temperature T_0. The choice of atomic friction coefficients γ_i is important for the result we get: if the selected values are too small (loose coupling), temperature control is poor (for all $\gamma_i = 0$, we get classic MD and a microcanonical ensemble); if they are too

large (tight coupling), perturbations take over (limiting case for very large γ_i is Brownian dynamics).

Stochastic coupling (Andersen thermostat)

In this algorithm, first proposed by Andersen (Andersen, 1980), the classic Newton equation of motion is integrated.

$$\ddot{\mathbf{r}}_i(t) = m_i^{-1}\mathbf{F}_i(t) \tag{3.40}$$

The components of velocities at each time step are, however, assigned based on the Maxwell-Boltzmann probability distribution.

$$p(\dot{r}_{i\mu}) = \left(\frac{m_i}{2\pi k_B T}\right)^{\frac{1}{2}} \exp\left(-\frac{m_i \dot{r}_{i\mu}^2}{k_B T}\right) \tag{3.41}$$

The intervals between velocity reassignments are also random with the following distribution, with reassignment frequency α.

$$p(\tau) = \alpha \exp(-\alpha t) \tag{3.42}$$

This approach algorithm mimics the random collisions of atoms with the particles of a bath at temperature T_0. The Andersen algorithm generates a canonical distribution of microstates and is non-deterministic, time-irreversible and non-smooth due to the velocities being randomly reassigned. Similarly to SD and the choice of γ_i, the choice of collision frequency α is crucial. Small values (poor coupling) provide poor temperature control and $\alpha = 0$ leads to MD. Too large values of α (tight coupling) perturb heavily the dynamics of the system.

Temperature constraining (Hoover-Evans, Woodcock and other thermostats)

The previously-mentioned methods employed soft boundary conditions in regards to temperature as they allowed temperature fluctuations. The following methods introduce temperature constraining, meaning the instantaneous temperature $\mathcal{T}$ of the system is going to be fixed to the bath temperature T_0 with no fluctuations.

Hoover (Hoover et al., 1982) and Evans (Evans, 1983) simultaneously proposed an algorithm which introduces a constrain on the temperature in the following form.

$$\mathcal{T}\left(t + \frac{\Delta t}{2}\right) = \mathcal{T}\left(t - \frac{\Delta t}{2}\right) \tag{3.43}$$

Theoretically, the temperature should be fixed at all times; however, in practice, the constraining condition is only enforced by zeroing the temperature derivative. And since the bath temperature T_0 is not explicitly used in the condition, numerical inaccuracies accumulate, leading to temperature drift. The Hoover-Evans algorithm generates a canonical ensemble of configurations.

Woodcock (Woodcock, 1971) chose a different condition to conserve the temperature.

$$\mathcal{T}\left(t + \frac{\Delta t}{2}\right) = \frac{N_{df} - 1}{N_{df}} T_0 \qquad (3.44)$$

The equation of motion corresponding to the Woodcock thermostat is rigorously equivalent to that of the Hoover-Evans thermostat, so it generates a canonical ensemble of configurations as well. However, the algorithms differ numerically and since, in this case, the temperature T_0 is explicitly part of the constraining condition, there is no risk of temperature drift.

There are other, similar algorithms based on temperature constraining, for example the Haile-Gupta (Haile and Gupta, 1983) thermostat, which, however, does not generate a canonical ensemble.

Equations of motions generated by temperature constraining algorithms are smooth, deterministic and time-irreversible. There are no fluctuations in kinetic energy which may lead to inaccurate dynamics.

Weak coupling (Berendsen thermostat)

Berendsen (Berendsen et al., 1984) modified the Langevin equation to remove local temperature coupling through stochastic collisions while retaining global coupling. This is equivalent to setting the following condition on the instantaneous temperature derivative $\dot{\mathcal{T}}(t)$.

$$\dot{\mathcal{T}}(t) = \tau_B^{-1}\left[T_0 - \mathcal{T}(t)\right] \qquad (3.45)$$

The constant τ_B represents temperature relaxation time but in reality, it is a parameter which is adjusted to control the thermostat. For $\tau_B \to \infty$, we receive classing MD, sampling a microcanonical ensemble. Large values (loose coupling) of τ_B may also cause temperature drift. If τ_B are too small (tight coupling), the fluctuations in temperature are unrealistically small and for $\tau_B = \Delta t$, we receive the Woodcock thermostat, which allows no fluctuations at all.

The equation of motion of the Berendsen algorithm is smooth, deterministic and time-irreversible. The algorithm does not generate a canonical ensemble.

Extended system method (Nosé-Hoover thermostat)

First proposed by Nosé (Nosé, 1984a) and then simplified simultaneously by Nosé (Nosé, 1984b) and Hoover (Hoover, 1985), this algorithm is based on the idea of extending the real system by adding an artificial variable $\tilde{s}$ which plays the role of a time-scaling parameter. The timescale of the extended system is stretched out so that $\mathrm{d}t = \tilde{s}_{-1}\left(\tilde{t}\right)\mathrm{d}\tilde{t}$ (t is time in the real system and $\tilde{t}$ in the extended one). This means that coordinates are identical in both systems, but velocities are amplified by $\tilde{s}_{-1}$ in the extended system.

The resulting equations of motion sample a microcanonical ensemble in the extended system with constant extended system energy E_e. In the real system,

	MD	MC	SD	A	HE	W	HG	B	NH
Deterministic	+	-	-	-	+	+	+	+	+
Time-reversible	+	-	-	-	+	+	+	-	+
Smooth	+	-	+	-	+	+	+	+	+
Energy drift	+	-	-	-	+	-	-	-	-
Oscillations	-	-	-	-	-	-	-	-	+
External d. o. f.	+	+	-	-	+	+	+	+	+
Constrained $\mathcal{K}$	-	-	-	-	+	+	+	-	-
Canonical in $\mathcal{H}$	-	-	+	+	-	-	-	-	+
Canonical in $\mathcal{U}$	-	+	+	+	+	+	-	-	+
Dynamics	++	- -	++	-	-	-	-	+	++

Table 3.2: Comparison of temperature control algorithms: Column headers: **MD** – molecular dynamics, **MC** – Monte Carlo, **SD** – stochastic dynamics, **A** – MD with Andersen thermostat, **HE** – MD with Hoover-Evans thermostat, **W** – MD with Woodcock thermostat, **HG** – MD with Haile-Gupta thermostat, **B** – MD with Berendsen thermostat, **NH** – MD with Nosé-Hoover thermostat. Line headers: **Deterministic** – trajectory is deterministic, **Time-reversible** – equation of motion is time-reversible; **Smooth** – velocity trajectory is continuous; **Energy drift** – possible energy and temperature drift due to accumulation of numerical errors; **Oscillations** – possible oscillatory behaviour of temperature dynamics; **External d. o. f.** – some external degrees of freedom are not coupled with the internal degrees of freedom; **Constrained** $\mathcal{K}$ – no kinetic energy fluctuations; **Canonical in** $\mathcal{H}$ – generates a canonical distribution of microstates; **Canonical in** $\mathcal{U}$ – generates a canonical distribution of configurations; **Dynamics** – dynamical information is absent (- -), likely to be unrealistic due to constrained temperature or non-smooth trajectory (-), moderately realistic – smooth trajectory, but temperature fluctuations of incorrect magnitude (+), or realistic – smooth trajectory, correct magnitude of temperature fluctuations (++).

however, energy fluctuates, heat is transferred between the bath and the real system (if the extended velocity $\dot{\tilde{s}}_{-1} > 0$, heat flows out of the system and for $\dot{\tilde{s}}_{-1} < 0$ into the system) and a canonical ensemble is sampled. The modifiable parameter in the Nosé-Hoover thermostat is the fictitious mass Q. In the limit of $Q \to \infty$, we get classical MD with a microcanonical ensemble. Too large values of Q (loose coupling) provide poor temperature control, while too small values may cause high-frequency temperature oscillations. The equation of motion is smooth, deterministic and time-reversible.

Table 3.2, adapted from (Hünenberger, 2005) shows a comparison of the above-mentioned algorithms for controlling temperature during a molecular dynamics simulation.

3.3.4. Barostats

In the previous chapter, we have been focusing on algorithms describing systems with constant temperature and volume and thus generating the canonical (NVT) ensemble. For some simulations, it is advantageous to use the Gibbs (NPT) ensemble and so a pressure control algorithm, a barostat, is used.

In MD simulations, the pressure P is usually calculated with the following formula.

$$P = \frac{Nk_BT}{V} + \frac{2}{3}\frac{\langle T \rangle}{V} \tag{3.46}$$

The first term comes from the equation of state of the ideal gas and the second term makes use of the virial theorem (Clausius, 1870). According to this theorem, the average total kinetic energy $\langle T \rangle$ of a system of particles with coordinates $\mathbf{r}_i$ depends on the forces $\mathbf{F}_i$ acting on these particles.

$$\langle T \rangle = \frac{1}{2}\sum_{i=1}^{N} \mathbf{r}_i \cdot \mathbf{F}_i \tag{3.47}$$

In a system with periodic boundary conditions, particles interact not only with others in the unit cell but also with the particles of the translated neighbouring cells, so the last equation is slightly modified.

$$\langle T \rangle = \frac{1}{2}\sum_{i>1} \mathbf{r}_{ij} \cdot \mathbf{F}_{ij} \tag{3.48}$$

Berendsen method

The Berendsen algorithm (Berendsen et al., 1984) couples the investigated system to a pressure bath with pressure P_0. There are two parameters determining the

strength of coupling, the compressibility γ of the system and relaxation time τ. Using these parameters a scaling factor μ by which the coordinates of each atom are adjusted at timestep Δt is defined.

$$\mu = \left(1 + \frac{\Delta t}{\tau}\gamma\left[P - P_0\right]\right)^{\frac{1}{3}} \tag{3.49}$$

Each of the components is adjusted by the same factor, so the size of the unit cell is changed, but its shape stays the same. It is therefore not suitable for any systems where we would expect the shape of the cell to change, e. g. crystal phase transitions.

Andersen method

The idea behind Andersen's (Andersen, 1980) pressure control is to treat the volume of the cell V as a dynamic variable. The Lagrangian of the system is modified to include a kinetic energy term with a parametric mass M and a potential term with a potential based on an external pressure P_0.

As stated above, the volume of the systems unit cell does change. However, the shape stays the same, just like with the Berendsen barostat. This is useful for liquid simulations but it means we cannot simulate anisotropic pressure with either method.

Parrinello-Rahman method

If one wishes to study materials under anisotropic stress, the Parrinello-Rahman (Parrinello and Rahman, 1981) method can be employed. It is an extension of the Andersen method and similarly to it, a kinetic energy term, based on a mass-like parameter W, is included in the Lagrangian. An elastic energy term related to the pressure and volume of the system is also included. Derived from the Lagrangian, the cell vectors are allowed to change freely, and thus both the size and shape of the unit cell can change. The rate of change depends on the parameter W. The larger it is, the slower the evolution of the system, and $W \to \infty$ produces a system of constant volume. Too small values of W do not give the system enough time for equilibration and may lead to periodic motions of the cell.

4. Experimental methods

Many different experimental methods can be used to study LDH with various intercalated anions. For example, thermogravimetric analysis (TGA) (Roelofs et al., 2002), Fourier transform infrared spectroscopy (FTIR) (Shabanian et al., 2020), automated diffraction tomography (ADT) (Conterosito et al., 2015) or transmission electron microscopy (TEM) (Káfuňková et al., 2010). In the following section we will provide a short summary of two methods, the results of which were used as a reference for our simulations, powder X-ray diffraction (PXRD) and solid state nuclear magnetic resonance (SSNMR).

4.1. Powder X-ray diffraction

X-ray diffraction (XRD) techniques are the most common method for performing crystallographic analysis, or the determination of what atoms, in what amounts and at what positions are in a unit cell of a crystal. The investigated specimen can be either in the form of a monocrystal and then statistical methods of solving are used or in the form of a powder (which is what we will focus on in this section), in which case molecular simulations methods are a useful tool for powder solving. Apart from the kind of atoms and their positions and amounts, the diffraction is mainly determined by the periodicity of spatial ordering of the atoms in the crystal.

4.1.1. Principles of diffraction

The diffraction pattern itself is not reminiscent of the actual structure of the crystal; instead, it is based on the so-called reciprocal crystal lattice, which is a Fourier transform of the direct (real) crystal lattice.

From a mathematical point of view, the crystal lattice is a Bravais lattice, an infinite array of discrete points generated by a set of discrete translation operations. In three-dimensional space, it can be described by a linear combination of primitive vectors $\mathbf{a}_1$, $\mathbf{a}_2$ and $\mathbf{a}_3$ (n_1, n_2, n_3 are integers).

$$\mathbf{R} = n_1\mathbf{a}_1 + n_2\mathbf{a}_2 + n_3\mathbf{a}_3 \tag{4.1}$$

The way to construct the reciprocal lattice is to choose a point of origin and from this point to construct a line perpendicular to a lattice plane (which is any plane containing at least three noncollinear points of the lattice). On this line we, construct a point of the reciprocal lattice at a distance $1/d_{hkl}$ from the origin,
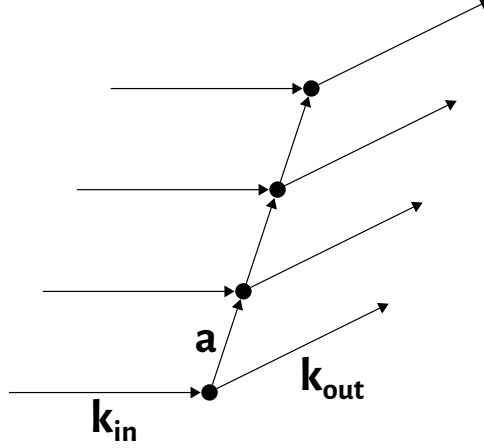
Figure 4.1: Scattering of radiation on a simple line of atoms.

where d_{hkl} is the interplanar distance in direct space (meaning it is the distance between two planes which intersect the unit cell at coordinates $[1/h, 1/k, 1/l]$). Repeating this process for all lattice planes (hkl), we receive the reciprocal plane, which can be described using a linear combination of reciprocal primitive vectors $\mathbf{b}_1$, $\mathbf{b}_2$ and $\mathbf{b}_3$ (h, k, l are integers, so-called Miller indices).

$$\mathbf{G}_{hkl} = h\mathbf{b}_1 + k\mathbf{b}_2 + l\mathbf{b}_3 \tag{4.2}$$

The relationship between the primitive vectors and the reciprocal primitive vectors is as follows.

$$\mathbf{a}_i \cdot \mathbf{b}_j = \delta_{ij} \tag{4.3}$$

Figure 4.1 shows radiation scattering on a line of atoms. For scattering to occur on a three-dimensional lattice, the wavevector of the incident radiation $\mathbf{k}_{in}$ and wavevector of the outgoing radiation $\mathbf{k}_{out}$ must satisfy the Laue equations.

$$(\mathbf{k}_{out} - \mathbf{k}_{in}) \cdot \mathbf{a}_1 = h \tag{4.4}$$

$$(\mathbf{k}_{out} - \mathbf{k}_{in}) \cdot \mathbf{a}_2 = k \tag{4.5}$$

$$(\mathbf{k}_{out} - \mathbf{k}_{in}) \cdot \mathbf{a}_3 = l \tag{4.6}$$

The difference between the incident and outgoing wavevectors is called the scattering vector $\Delta\mathbf{k}$ and it is a reciprocal lattice vector, so it can be defined in the same way as $\mathbf{G}_{hkl}$ above. A graphical representation of this situation is called the Ewald construction and is shown in Figure 4.2. In it, we construct a sphere with a radius of $1/\lambda$, called the Ewald sphere. In the centre of the Ewald sphere
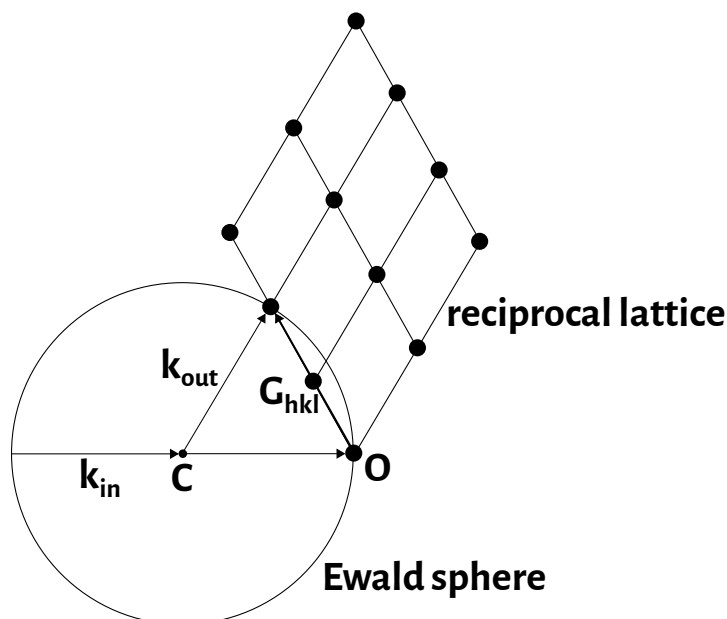
Figure 4.2: The Ewald construction: C – diffracting crystal, O – point of origin of the reciprocal lattice.

lies the diffracting crystal, and at the point of the sphere where the incident beam leaves the sphere, we place the origin of the reciprocal lattice. Then, constructing the reciprocal lattice from there, if a reciprocal lattice point *hkl* lies on the Ewald sphere, the conditions given by the Laue equations are satisfied and the diffracted beam leaves the Ewald sphere through this point. From this, we can see that the diffraction image corresponds to the reciprocal lattice (Ewald, 1969).

Building on the Ewald construction, Figure 4.3 shows an interpretation of Laue diffraction called Bragg's law after Lawrence Bragg and his father, William Henry Bragg, who first proposed it in 1913 (Bragg and Bragg, 1913). In it, we can see the crystal plane (*hkl*) to which the vector $\mathbf{G}_{hkl}$ is perpendicular. The incident beam of radiation appears to be reflected from the plane (*hkl*), which is the reason why in X-ray diffraction we speak about reflections. The angle θ is called Bragg angle and 2θ is called diffraction angle. Bragg's law gives us the relationship between the angle θ, the planar distance d_{hkl} and the wavelength of the incident radiation λ.

$$2d_{hkl}\sin\theta = n\lambda \tag{4.7}$$

The integer n signifies the order of the observed reflection (Kittel, 2005).
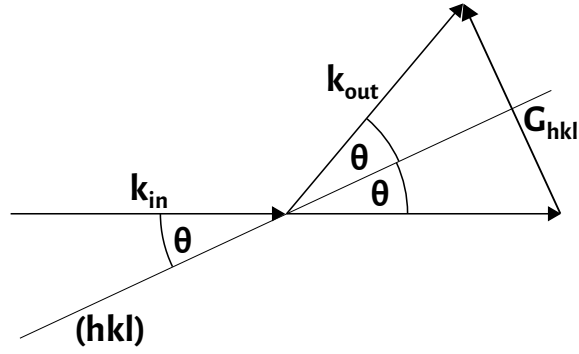
Figure 4.3: Bragg's law.

4.1.2. Powder diffraction

The diffraction pattern looks as the points of the reciprocal lattice if we are working with a monocrystal. If the sample, which we are studying, is made up of many small crystals of different orientations, i. e. a powder, all the possible reciprocal lattices have to be overlapped and the diffraction pattern takes the shape of concentric spheres with their centre in the origin of the lattice as is shown in Figure 4.4. The intersection of these spheres and the Ewald sphere are circles. The same pattern would be observed if a monocrystal was continuously irradiated while being rotated in all different directions.

In a powder diffraction experiment, the detector moves along a circle around the sample and the diffraction angles 2θ at which reflections appear are noted down. Using Bragg's law, the planar distances can easily be calculated from these angles. However, the diffractogram gives us no information about the orientation of the planes. Other complications include overlapping of planar distances, preferred orientation of crystals in a sample, absorption of X-rays on the samples surfaces or partially disordered samples. Due to these complications, the amount of information that can be attained form a powder diffraction measurement depends on the properties of the sample itself as well as the number of reflections measured (Giacovazzo, 1992). Various techniques for analysing powder diffractograms exist (Etter and Dinnebier, 2014), which include not only the post processing of the measured data (for example Rietveld refinement (Rietveld, 1969)) but also the preparation of the sample itself (Moore and Reynolds Jr., 1997).

4.1.3. X-ray diffraction of layered double hydroxides

X-ray diffraction is a useful tool for analysing layered LDH. As LDH do not form large monocrystals, powder XRD techniques are used. The key parameter of an
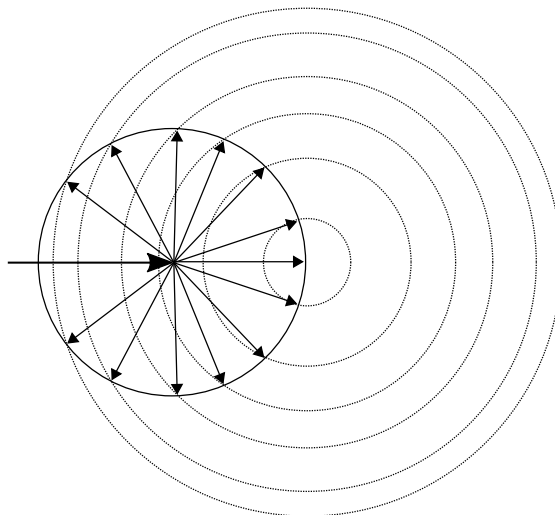
Figure 4.4: The construction of a diffraction pattern of a powder sample.

LDH structure is the basal spacing, i. e. the distance between the hydroxide layers, so that is often the main focus of PXRD experiments on LDH. However, many reflections can be observed in the diffractogram and further details about the structure can be inferred from the data. Rietveld refinement can be used (Bellotto et al., 1996), but more often, a trial-and-error approach is used to index individual peaks and determine space group and crystal axes. A model of a structure is built and a diffraction pattern is calculated, which is then compared with the measured experimental results. The model is then refined until the calculated diffractogram matches the measured one. An advantage of this approach is that it can easily be used even for defective structures which would be impossible to analyse using Rietveld refinement or similar methods (Rives, 2001).

4.2. Solid state nuclear magnetic resonance

Nuclear magnetic resonance (NMR) is a useful technique for determining the chemical structure of various compounds. It is based on observing the changes in spin orientation of a nucleus when put inside a magnetic field. The main phenomenon observed in NMR spectra is so called chemical shift, most often due to electron shielding. Other phenomena include J-coupling, which causes the observed peaks to split into multiple peaks, and dipolar as well as quadripolar couplings (Reif et al., 2021).

The basic principles of NMR are the same for liquid-state NMR and solid-state NMR (SSNMR), there are, however, some key differences which we will address.

4.2.1. Principles of nuclear magnetic resonance

In order for an atomic nucleus to exhibit any magnetic resonance effects, its overall spin must be non-zero. The overall spin of a nucleus is given by the sum of the nucleons it is made up of, and since these generally tend to order themselves with spins anti-parallel to each other, it can only be non-zero if there is an odd number of protons or neutrons (or of both). Two examples of nuclides that have this property and that are most commonly used in NMR spectroscopy are ^{1}H and ^{13}C.

The reason why a non-zero spin is necessary for interactions with a magnetic field is the relationship between spin $\mathbf{S}$ and magnetic dipole moment $\boldsymbol{\mu}$, which is a simple linear relationship with the gyromagnetic constant γ:

$$\boldsymbol{\mu} = \gamma \mathbf{S} \tag{4.8}$$

The same relationship holds for each of the spatial components of $\mathbf{S}$ and $\boldsymbol{\mu}$. Since nuclear spin is quantised, the component along the z-axis of an applied magnetic field can only obtain the values of integer or half-integer multiples of reduced Planck constant $\hbar$, with the integer or half-integer in question being the magnetic quantum number m.

$$\mu_z = \gamma S_z = \gamma m \hbar \tag{4.9}$$

The energy of a magnetic dipole moment $\boldsymbol{\mu}$ in a magnetic field $\mathbf{B}_0 = (0, 0, B_0)$ aligned with the z-axis:

$$E = -\mu_z B_0 = -\gamma m \hbar B_0 \tag{4.10}$$

Both ^{1}H and ^{13}C, as well as many other nuclides, have a nuclear spin of $\frac{1}{2}$, and so the energy splits into two levels (this phenomenon is known as the Zeeman effect (Lodge, 1897), $m = \pm\frac{1}{2}$, with the spin aligning either with the magnetic field or against it. For most isotopes used in NMR, the gyromagnetic constant is positive and thus the lower energy state is the one with $m = \frac{1}{2}$. In thermal equilibrium, the lower energy level will be slightly more populated than the higher one which results in a net spin magnetisation along the magnetic field $\mathbf{B}_0$.

The spin magnetisation of an atom undergoes a precession around the magnetic field at the nucleus. For the applied magnetic field $\mathbf{B}_0$, this precession happens at a so-called Larmor frequency ω_L.

$$\omega_L = -\gamma B_0 \tag{4.11}$$

As we can see, the resonant Larmor frequency is dependent on $\mathbf{B}_0$ at the

position of the nucleus. The magnetic field is influenced by the surroundings of the nucleus and so, if we are able to detect small changes in the resonant frequency, we are able to gain an insight into the chemical composition as well as the spatial distribution of the measured sample.

If a radiofrequency (RF) pulse with a frequency very close to the Larmor precession interacts with the nucleus, the nuclei move from the lower energy state to the higher one and the magnetisation changes direction. When the nucleus returns back to the lower state, the transition energy is detected. The relaxation time plays an important role and RF pulses of different lengths are used to perform different types of NMR experiments.

The signal detected from the sample, as it is relaxing back to its state before the RF pulse, is detected in the form of induced oscillated voltage called free induction decay (FID). By performing Fourier transform, the signal is transformed to the frequency domain resulting in a spectrum of resonant frequencies which can then be analysed (Ernst, 1992).

4.2.2. Chemical shift

The quantity measured in NMR experiments is called chemical shift. It is calculated from the difference between the actual measured resonance frequency ν_{sample} of a sample and a resonance frequency ν_{ref} of a reference compound.

$$\delta = \frac{\nu_{sample} - \nu_{ref}}{\nu_{ref}} \qquad (4.12)$$

The unit used is parts per million (ppm) due to the fact that the frequencies in the numerator are usually written in Hz and the frequency in the denominator in MHz. The most commonly used reference compounds are tetramethylsilane (TMS), trimethylsilylpropanoic acid (TMSP) or sodium trimethylsilylpropane-sulfonate (DSS), a schematic representation of them is shown in Figure 4.5. TMS is very suitable for use as a standard reference compound due to the fact that all its twelve hydrogens are equivalent thanks to the molecule's symmetry, and so its NMR spectrum consists of a single peak which allows it to be easily identified for calibration. The same goes for the four carbons, so this property holds up for both ^{1}H and ^{13}C NMR. Another advantage is that it evaporates easily, so it can be separated from the sample after the NMR measurement is finished (Mohrig et al., 2006). However, TMS is not soluble in water, so for NMR experiments where water is used as a solvent, TMSP or DSS are used. TMSP is more easily soluble in water than DSS, but DSS has the advantage that its NMR response is less sensitive to changes in pH (De Marco, 1977).

There are several effects that influence the chemical shift detected in different
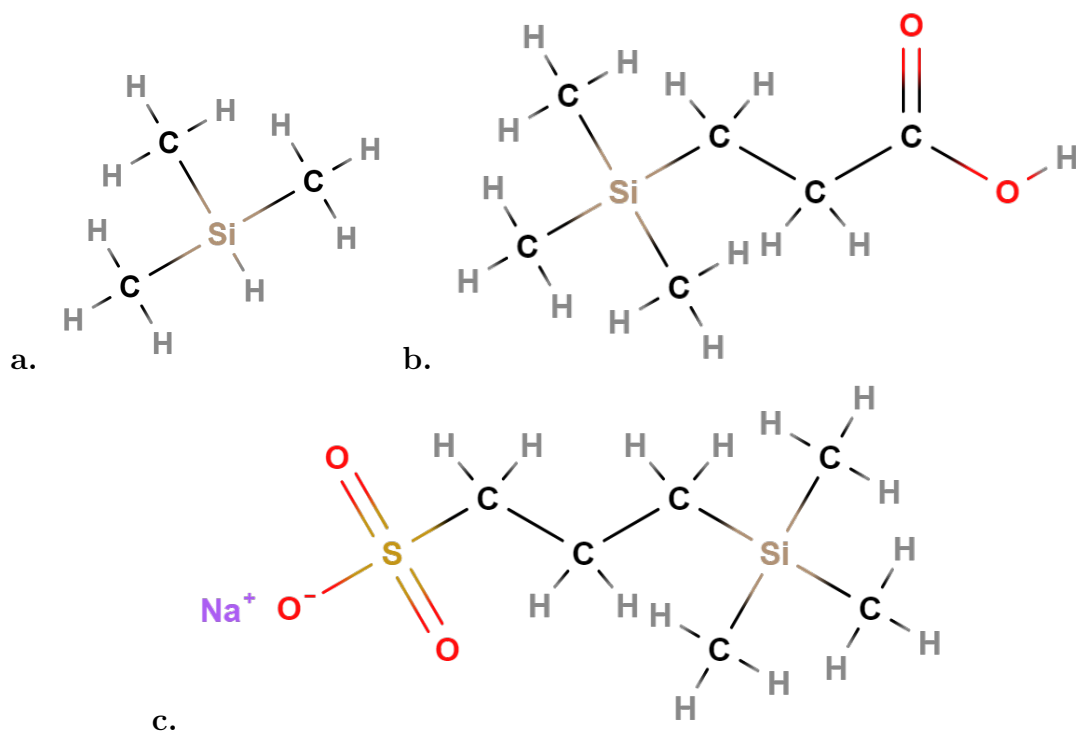
Figure 4.5: The chemical structure of the most commonly used NMR reference compounds: **a.** TMS; **b.** TMSP; **c.** DSS (all created using `https://molview.org/`).

molecules, the most prominent are chemical shielding, J-coupling and dipolar coupling.

Chemical shielding is the main effect observed in NMR spectroscopy as it determines the position of the observed peaks. As mentioned earlier, the resonant frequency of a measured nucleus is dependent on the magnetic field acting on the nucleus. However, this magnetic field is not exactly equal to the applied field $\mathbf{B_0}$ as any charges in the vicinity of the measured nucleus influence the size of the field. In particular, the electron density surrounding the nucleus interacts with the magnetic field, "shielding" the nucleus from its effect and slightly lowering the resonance frequency.

J-coupling, or spin-spin coupling, refers to the interaction between nuclear spins mediated through chemical bonds. For example, in ^{1}H spectroscopy where the nuclear spin is $\pm\frac{1}{2}$, a system of two nuclei has four possible states: $\left(-\frac{1}{2}, -\frac{1}{2}\right)$, $\left(-\frac{1}{2}, +\frac{1}{2}\right)$, $\left(+\frac{1}{2}, -\frac{1}{2}\right)$ and $\left(+\frac{1}{2}, +\frac{1}{2}\right)$. The second and third state have the same energy resulting in a system with three energy levels, with the middle one being twice as populated as the other two. Therefore, the NMR peak splits into a triplet, with the intensities of the sub-peaks having the ratio 1:2:1. The situation is analogous for a higher number of interacting spins, with the ratios following the rows of a Pascal triangle, i. e. three spins result in a 1:3:3:1 quadruplet, four

spins in a 1:4:6:4:1 quintuplet and so on. For nuclei with a higher spin than $\frac{1}{2}$, for example ^{13}C, the splitting is more complicated.

4.2.3. Magic-angle spinning

The NMR phenomenon is the same in solids as in liquids, however, there is one difference when measuring NMR spectra. Anisotropic effects which are averaged to zero in liquid samples due to the Brownian motion of the molecules, are present in a solid sample and greatly influence the resulting NMR spectrum. On top of the chemical shift anisotropy, dipolar and quadrupolar interactions between spins also further broaden the peaks in an SSNMR spectrum. To avoid or at least lower the influence of these effects, so called magic-angle spinning (MAS) is introduced (Andrew et al., 1958).

The dipolar interaction is dependent on the angle θ between the internuclear vector and the external magnetic field vector. This dependence is in the form $3\cos^2\theta - 1$ and thus, the interaction is equal to zero for the so-called magic angle

$$\theta_m = \arccos\sqrt{\frac{1}{3}} = 54°44'. \tag{4.13}$$

To ensure that all nuclei in the sample fulfil this condition is clearly impossible. However, the same effect can be achieved by spinning the sample at a high enough frequency around an axis tilted by the magic angle θ_m (with respect to the magnetic field). The frequency needs to be comparable to the speed of the interaction which means the used frequencies are at the order of 10^4–10^5 Hz. The dipolar interaction is removed from the NMR spectrum, leaving behind only a set of sidebands which are separated from the resonance frequency by a multiple of the spinning frequency. The quadrupolar interaction is partially averaged out by the MAS while the anisotropy of the chemical shift is averaged out completely and its contribution is removed from the NMR spectrum.

4.2.4. Two-dimensional nuclear magnetic resonance

Even though a simple NMR spectrum can provide a lot of information about the structure of a sample, there is still more information to be gained using an NMR experiment, especially regarding interactions between nuclei. This information can be utilised by the two-dimensional nuclear magnetic resonance (2D NMR) experiment. This also solves the problem which can arise for larger systems, that the NMR spectrum contains many overlapping peaks which are difficult to distinguish. By adding another dimension to the spectrum, it often becomes more easily readable and interpretable.

There are many different types of 2D NMR experiments, but they can be divided into two basic categories. Homonuclear 2D experiments utilise one type of NMR (e. g. ^{1}H or ^{13}C), while heteronuclear experiments focus on the interactions between two different nuclei. The specifics of each method differ but most consist of four stages. First, a series of RF pulses is used to establish coherence; then, after a certain evolution time during which the nuclear spins rotate freely, another series of pulses is applied to manipulate the coherence in the desired manner; and lastly, the FID signal is detected during the detection period. The 2D spectrum is gained by detecting a series of signals for different evolution times. After performing a two-dimensional Fourier transform on the recorded signals, a so-called correlation map is gained with resonant frequencies as the units on the x and y axes (Aue et al., 1976).

In homonuclear 2D NMR spectroscopy, the diagonal of a correlation map is just the same as a simple 1D NMR spectrum and contains the same information about chemical shielding and J-coupling. The off-diagonal peaks, called cross peaks, contain information about coupling between different nuclei. The most common types of 2D NMR spectroscopy include correlation spectroscopy (COSY), total correlation spectroscopy (TOCSY) or nuclear Overhauser effect spectroscopy (NOESY), which utilises the transfer of nuclear spin polarisation between non-bonded atoms (Overhauser, 1953).

In heteronuclear 2D NMR, each of the axes relates to a different type of nucleus, and therefore, the correlation map does not contain any diagonal peaks, all peaks observed are cross peaks, arising from various interactions between the nuclei of two different types. An example of a heteronuclear 2D NMR method is heteronuclear single-quantum correlation spectroscopy (HSQC) which detects interactions between atoms of two different types connected by one bond (Keeler, 2010).

5. Results and discussion

5.1. Models' preparation

5.1.1. Atorvastatin

An atorvastatin anion was built in Materials Studio. Then, the Conformers module was used to find a conformer with the lowest energy. During this search, Conformers rotated each of the single bonds in the molecule at 60-degree increments and calculated energy after each rotation. After selecting the lowest-energy conformer, Materials Studio's module Forcite was used to optimise the molecule's geometry. The resulting optimised atorvastatin anion is shown in Figure 5.1.

5.1.2. Water and anions

Similarly to atorvastatin, H_2O molecule and NO_3^- anion were built in Materials Studio. Since they are simple, small molecules without multiple possible conformations, there was no need to use the Conformers module and molecules were optimized straight away using the Forcite module.
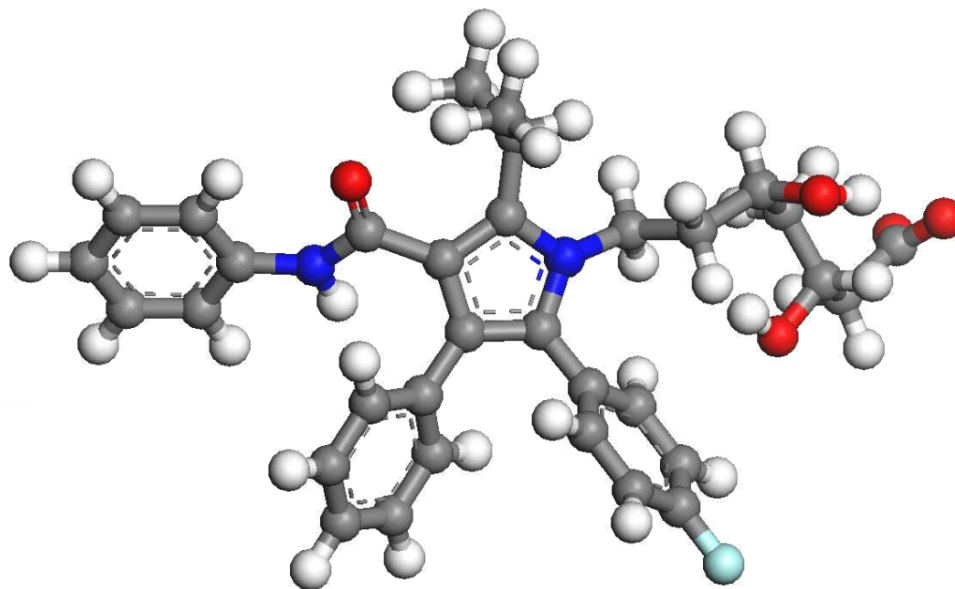
Figure 5.1: The optimised structure of atorvastatin, built in Materials Studio and optimised using the Conformers and Forcite modules. Colour-coding: carbon – grey; hydrogen – white; oxygen – red; nitrogen – blue; flourine – light blue.

Space group	a_0	b_0	c_0	α	β	γ
R-3m	0.307598 nm	0.307598 nm	2.32048 nm	90°	90°	120°

Table 5.1: Lattice parameters of LDH from (Veteška, 2009).

5.1.3. LDH

The crystalline structure of LDH was built using Materials Studio's Build Crystal function. Lattice parameters used come from (Veteška, 2009) and are shown in Table 5.1. Atoms were placed into this lattice at the following coordinates: Mg at $x/a = y/b = z/c = 0.0$; O at $x/a = y/b = 0.0$, $z/c = 0.377$.

After the unit cell was built, the *Build Supercell* functionality was used to create a $6a_0 \times 6b_0 \times 3c_0$ supercell, resulting in a structure with 3 layers of 36 magnesium cations each. As we wanted to build a structure with a 2:1 molar ratio of magnesium to aluminium, 12 atoms of magnesium from each layer were then manually replaced with aluminium. The atoms to be replaced were chosen in such a way that each Al cation is surrounded by six Mg cations (Sideris et al., 2008) as shown in Figure 5.2. From this figure, we can also see that such a structure possesses a translational symmetry in all directions, and therefore our 6×6 structure, if replicated by the Materials Studio software in each direction, is a good approximation for a large structure.
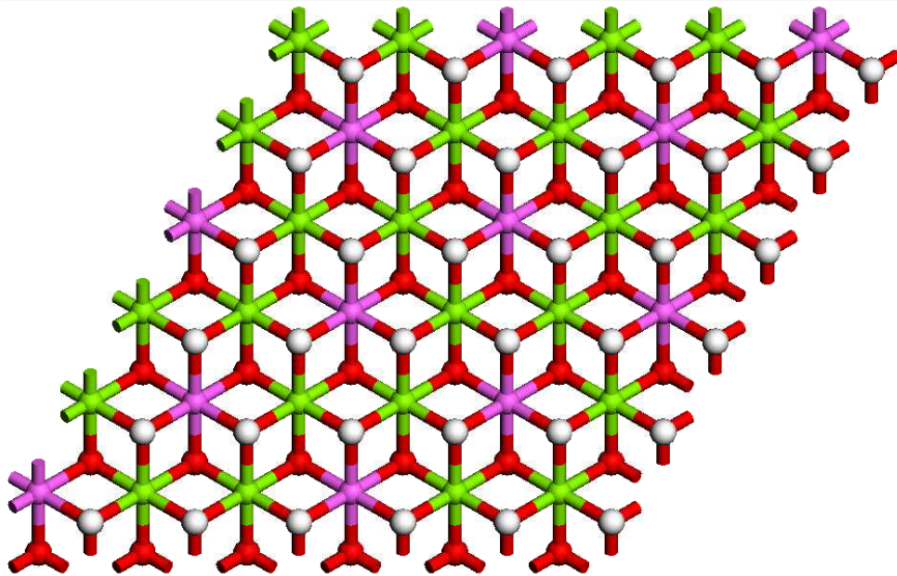
Figure 5.2: One layer of Mg$_2$Al LDH using the ball-and-stick model, viewed along the *c*-axis: Magnesium atoms are shown in green, aluminium atoms in blue, oxygen atoms in red and hydrogen atoms in white. A regular ordering of Mg and Al atoms was chosen based on previously reported experimental findings (Sideris et al., 2008).
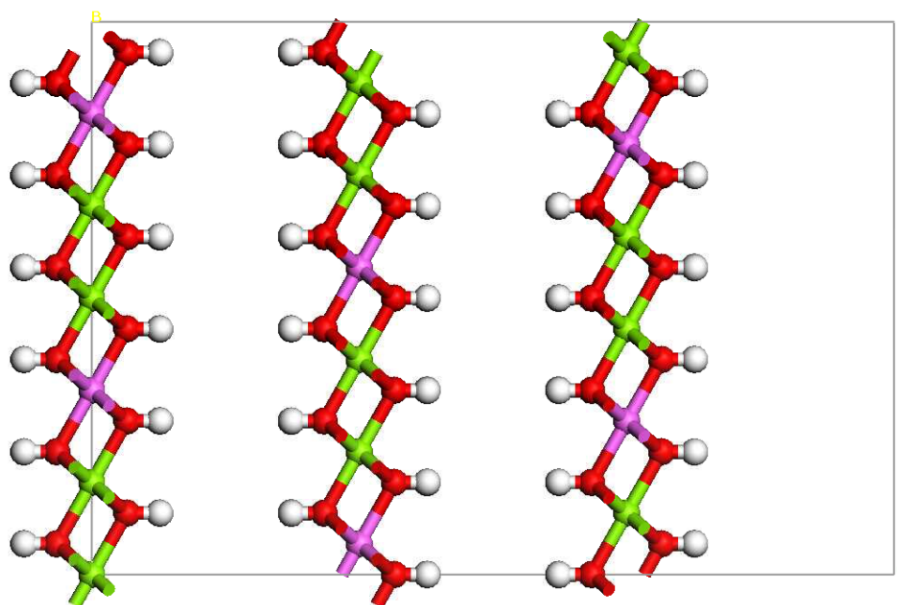
Figure 5.3: A starting model of Mg_2Al LDH before the basal spacing was adjusted and atorvastatin anions together with water molecules and nitrates anions were intercalated. Magnesium atoms are shown in green, aluminium atoms in blue, oxygen atoms in red and hydrogen atoms in white; the borders of the unit supercell are shown in grey.

The next step was to add hydrogen atoms to the structure. These were added manually, each hydrogen atom was placed above an oxygen atom and connected using a single bond. A total of 216 hydrogen atoms were added to the model, 36 to each side of each of the layers. Since the placement of these atoms was done manually, the length and direction of the bonds needed to be optimised using the Forcite module. The charges were calculated using the *Modify... Charge* functionality in Materials Studio. As this requires the model to be overall neutral, 12 NO_3^- anions were inserted between each of the layers to compensate the 12e charge of each layer. After charge calculation, the charges were manually adjusted to make sure that the overall charge of each layer was 12e and the anions were removed. The resulting structure is in Figure 5.3.

Three models were created from this structure, each with a different planar distance d_{003} between the LDH layers based on given atorvastatin concentrations from experimental findings sent by prof. František Kovanda (University of Chemistry and Technology, Prague). Due to the size limitations of our model, these experimental findings could not be replicated exactly as we always had to have an integer number of molecules in our LDH interlayer. The numbers were chosen so that they were as close to the experimental values as possible. Table 5.2 shows the differences between the three experimental structures and our three starting models, as well as the specific number of molecules that were used in our models.

Case	1		2		3	
	Experiment	Model	Experiment	Model	Experiment	Model
d_{003}	3.751 nm		3.808 nm		3.823 nm	
ATS/Al molar ratio	0.721	0.667	0.999	1.000	0.923	0.917
Amount of ATS	61.10 %	61.99 % (8 molecules)	75.80 %	73.19 % (12 molecules)	70.00 %	70.64 % (11 molecules)
Amount of H_2O	5.05 %	5.00 % (20 molecules)	3.64 %	3.54 % (18 molecules)	4.26 %	4.14 % (20 molecules)

Table 5.2: Experimental values from F. Kovanda and conditions of our starting models.

The desired planar distance d_{003} between the crystal layers was achieved by first modifying the lattice parameter c and then moving each of the layers accordingly, resulting in the distances noted down in Table 5.3.

5.1.4. Initial arrangements

For each of the three models, several different starting orientations of atorvastatin molecules were chosen, examples are shown in Figure 5.4.

Arrangement A was used only with the structure with basal spacing of 3.808 nm, it was not used with the other structures, because it took a very long time for it to reach convergence, and in the end, the result was very similar to the arrangement D. The remaining arrangements were used with all 3 models, resulting in a total number of 10 model systems, shown in Table 5.4.

Model	a	b	c	d_{003}
1	1.84559 nm	1.84559 nm	11.253 nm	3.751 nm
2	1.84559 nm	1.84559 nm	11.424 nm	3.808 nm
3	1.84559 nm	1.84559 nm	11.469 nm	3.823 nm

Table 5.3: Comparison between the basal spacing and lattice parameters of the three investigated models of $6a_0 \times 6b_0 \times 3c_0$ LDH.

5.2. Geometry optimisation

On every starting orientation of each of the models, an optimisation of geometry was performed using Materials Studio's Forcite module. The COMPASS (Sun, 1998) force field was used, the optimisation algorithm used in Materials Studio is called 'smart' and it is a combination of steepest descent at the beginning of optimisation and then it is switched to the conjugate gradient method. The final level of convergence was 0.001 kcal/mol for differences in energy and 0.5 kcal/mol/Åfor differences in force. For electrostatic interactions, Ewald summation was used (Wells and Chaffee, 2015), with an accuracy of 0.0001 kcal/mol and van der Waals interactions were cut off at a distance of 15.5 Å with a 1-Å spline and 0.5-Å buffer. The maximum number of iterations was set to 20,000 and if a model did not converge within 20,000 iterations, the optimisation was run again with the same parameters until convergence was reached.

There were several procedural rounds of geometry optimisations, all with the settings described above. In the first run, the LDH layers were kept fixed in positions by constraining their Cartesian coordinates and only the anions and water molecules were allowed to move. After reaching convergence with these
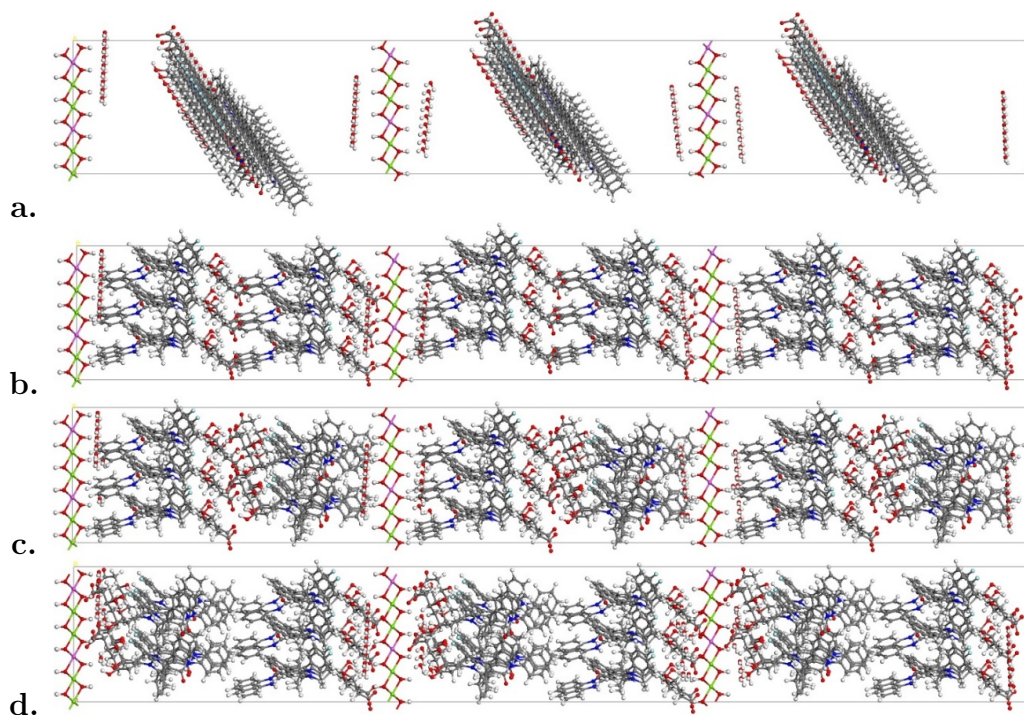
Figure 5.4: Initial orientations of atorvastatin molecules in LDH: **a.** Arrangement A – clustered; **b.** Arrangement B – all molecules ordered in the same direction, perpendicular to the LDH layers; **c.** Arrangement C – six molecules in one direction, six in the opposite direction, with the COO^- group in the middle; **d.** Arrangement D – six molecules in one direction, six in the opposite direction, with the COO^- groups pointed towards the LDH layers.

Model	Basal spacing	Atorvastatin orientation
1B	3.751 nm	all molecules ordered in the same direction, perpendicular to the LDH layers
1C	3.751 nm	six molecules in one direction, six in the opposite direction, with the COO^- group in the middle
1D	3.751 nm	six molecules in one direction, six in the opposite direction, with the COO^- groups pointed towards the LDH layers
2A	3.808 nm	clustered
2B	3.808 nm	all molecules ordered in the same direction, perpendicular to the LDH layers
2C	3.808 nm	six molecules in one direction, six in the opposite direction, with the COO^- group in the middle
2D	3.808 nm	six molecules in one direction, six in the opposite direction, with the COO^- groups pointed towards the LDH layers
3B	3.823 nm	all molecules ordered in the same direction, perpendicular to the LDH layers
3C	3.823 nm	six molecules in one direction, six in the opposite direction, with the COO^- group in the middle
3D	3.823 nm	six molecules in one direction, six in the opposite direction, with the COO^- groups pointed towards the LDH layers

Table 5.4: An overview of the initial LDH basal spacing and ATS anion orientations in the investigated models.

settings, the constrains of Cartesian coordinates on the atoms were removed, allowing them to move freely in the next optimisation run, but in this step, the LDH layers were assigned as motion groups, meaning they could only move as a whole and no interactions were calculated between the atoms that belong to the same LDH layer. In the following optimisation procedure, the cell was also optimised, allowing the cell parameters a, b, c as well as the angles α, β, γ to change freely. After this run of optimisation, the charges were calculated again and geometry optimisation was repeated. The resulting structures are shown in Figure 5.5 and the resulting parameters in Table 5.5.

After the geometry optimisations, the Reflex module in Materials Studio was

1B

1C

1D

2A

2B

2D

3B

3C

3D
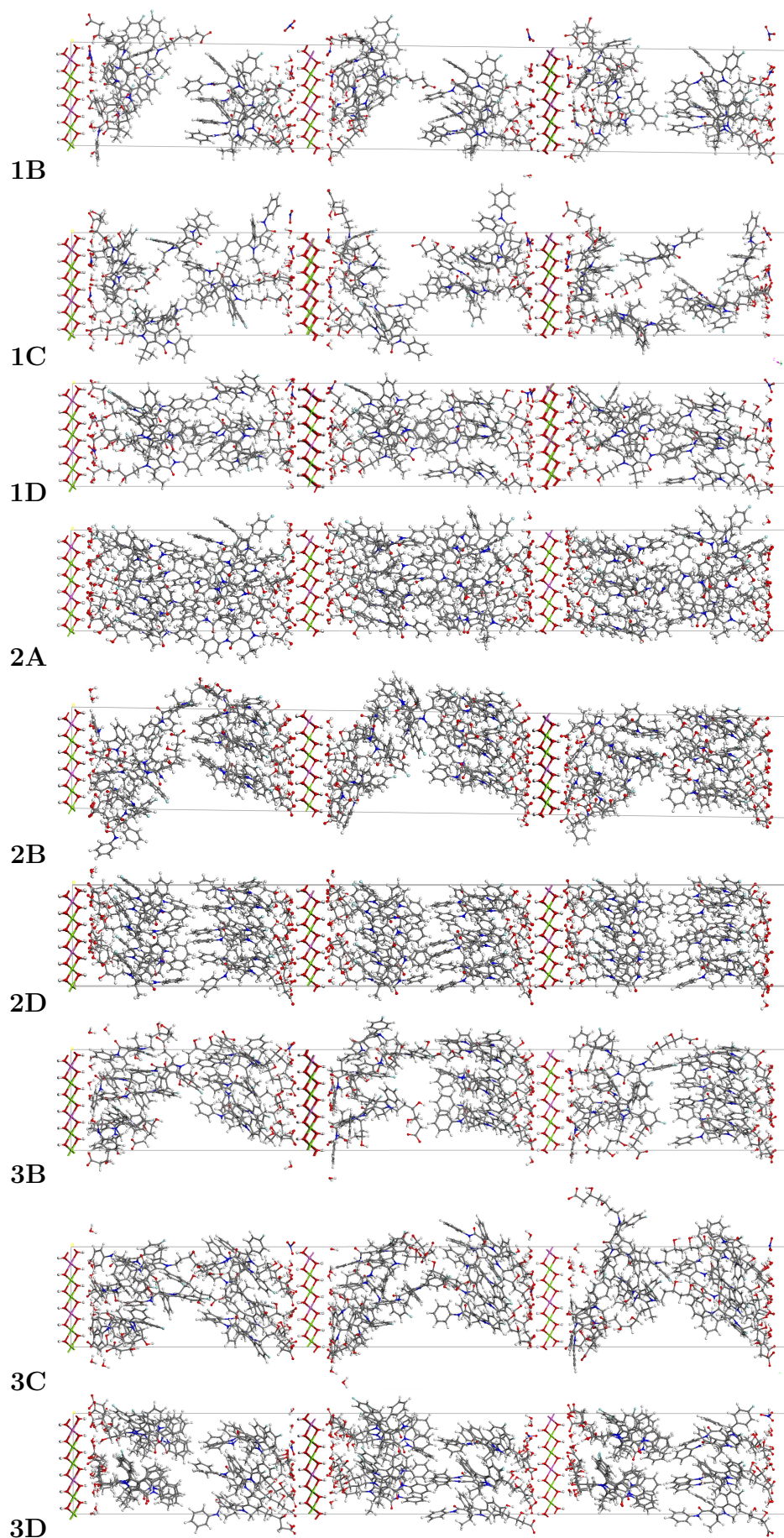
Figure 5.5: ATS-LDH models after geometry optimisations.

Model	Energy kcal/mol	a (nm)	b (nm)	c (nm)	α	β	γ	d_{003} (nm)
1B	-62497	1.85749	1.85346	11.25691	90.085°	91.030°	119.676°	3.751430
1C	-62243	1.84646	1.84601	11.25299	90.004°	90.004°	119.997°	3.750990
1D	-62534	1.84601	1.84664	11.25297	90.000°	90.007°	119.981°	3.750990
2A	-62917	1.84644	1.84637	11.42401	89.997°	89.998°	119.985°	3.808003
2B	-61177	1.85397	1.85832	11.41992	90.530°	90.264°	119.688°	3.806265
2D	-62295	1.84568	1.84568	11.42399	90.000°	90.001°	119.999°	3.807997
3B	-60102	1.84694	1.84684	11.46895	90.001°	90.001°	119.975°	3.822980
3C	-60464	1.84565	1.84561	11.46900	90.003°	90.002°	120.000°	3.822990
3D	-62335	1.84616	1.84569	11.46880	90.003°	90.005°	119.997°	3.822930

Table 5.5: Parameters of the ATS-LDH models after geometry optimisation.

used to simulate X-ray diffraction patterns of the resulting structures. The range of 2θ was set from 2° to 45° and the wavelength of the source of radiation was set to 1.7902 Å, corresponding to the K_α line of ^{27}Co to match the experimental conditions we are comparing our results to. In the calculated diffractograms, the first peak is the one we were mainly interested in, as it showed the basal spacing d_{003} mentioned above. The basal spacing, as well as the total energy and the lattice parameters for each of the models, are shown in Table 5.5. Model 2C is excluded from the table as it demonstrated unstable behaviour and did not reach convergence even after several repeated optimisation runs. Therefore, it was rejected and not used in the next stages of modelling.

5.3. Molecular dynamics

After geometry optimization, molecular dynamics was performed on the resulting structures 1B, 1C, 1D, 2A, 2B, 2D, 3B, 3C and 3D. The Forcite module in Materials Studio was used. The statistical ensemble was NVT, with random initial velocities, temperature 298 K, Nosé-Hoover thermostat (Nosé, 1984a,b; Hoover, 1985) with Q ratio 1.0, energy deviation tolerance of 5,000 kcal/mol, time step 1 fs. The total number of steps was 50,000, resulting in a total dynamics time of 50 ps. After every 10,000 frames (10 ps), the structure was optimised using the smart algorithm (combination of steepest descent and conjugate gradients) and convergence criteria of 0.001 kcal/mol for energy and 0.5 kcal/mol/Å for force, maximum of 5,000 iterations. In order to allow relaxation of the structure, no constraints were imposed on the lattice parameters, only LDH layers were designated as motion groups.

51

Model	Energy kcal/mol	a (nm)	b (nm)	c (nm)	α	β	γ	d_{003} (nm)
1B	-65235	1.85967	1.85504	11.13980	90.593°	93.147°	119.668°	3.704200
1C	-63388	1.84850	1.84672	11.25285	90.009°	90.012°	120.006°	3.750950
1D	-64040	1.84688	1.84720	11.25286	90.003°	89.999°	119.945°	3.750950
2A	-63210	1.84645	1.84639	11.42401	89.997°	89.998°	119.985°	3.808002
2B	-62815	1.85555	1.85949	11.41684	90.679°	90.335°	119.618°	3.805003
2D	-63498	1.84662	1.84662	11.41875	89.918°	90.091°	120.037°	3.806244
3B	-60621	1.84729	1.84729	11.46887	89.999°	89.997°	119.963°	3.822960
3C	-60827	1.84608	1.84565	11.46892	90.003°	90.010°	119.996°	3.822970
3D	-63294	1.84710	1.84580	11.46876	90.009°	89.994°	119.990°	3.822920

Table 5.6: Calculated parameters of the ATS-LDH models after the final molecular dynamics run.

Each run of the molecular dynamics procedure produced 6 optimised models. Out of those, the one with the lowest total energy was selected as the most probable optimal conformation. The resulting energy as well as other parameters are displayed in Table 5.6. Basal spacing d_{003} was once again calculated using the Reflex module with the same settings as mentioned above. Unfortunately, the Forcite module dynamics failed to keep the LDH layers strictly rigid and they have become slightly deformed during the MD procedure, as is shown in Figure 5.6. Therefore, in the future, MD calculations will need to be performed again to achieve fewer deformations of LDH layers.

5.4. Results and comparison with experiments

By analysing Figure 5.5, we can see that models 1B, 1C, 2B, 3B and 3C have quite disordered final states. There are gaps between the anions in the interlayer, suggesting these arrangements are not very stable. On the other hand, the models 1D, 2A, 2D and 3D are quite nearly ordered and with almost no gaps between the
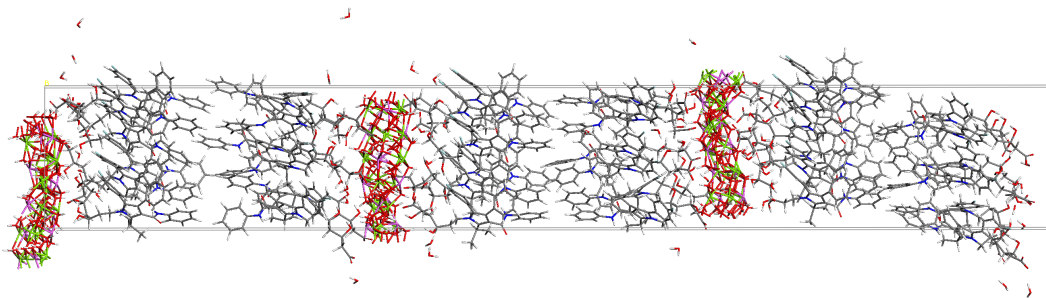
Figure 5.6: ATS-LDH model 2D after molecular dynamics.
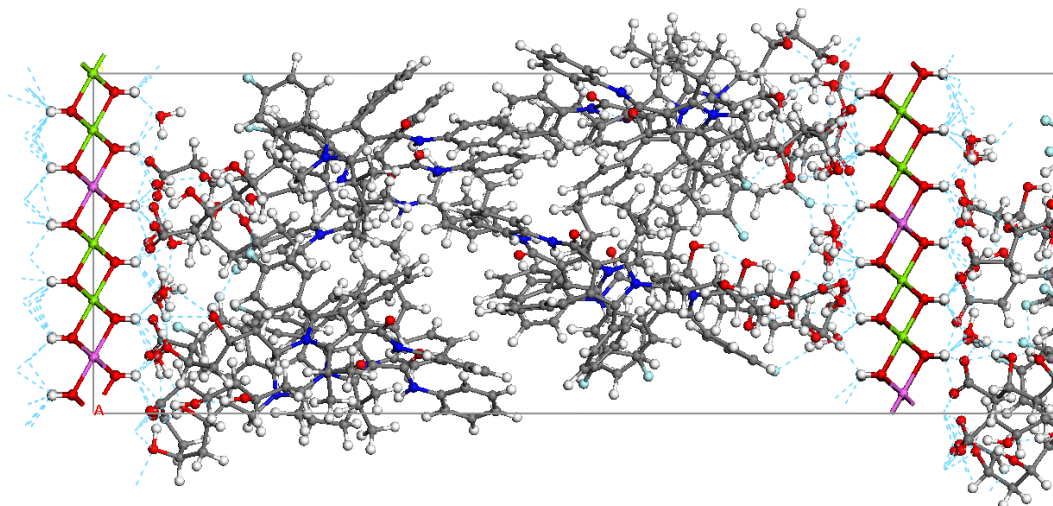
Figure 5.7: Detail from model 2A showing the hydrogen bonding between carboxyl groups of ATS and OH groups of LDH (in blue dashed line).

anions in the interlayer. Therefore, we conclude that the optimal arrangement is with the ATS anions placed so that their COO^- groups are facing the OH groups of the LDH layers. The anions interact with the LDH layers through hydrogen bonding as can be seen in Figure 5.7, which shows a detail of model 2A.

It is interesting to note, that even though model 2A started in a clustered arrangement, during the repeated optimisation runs, the anions shifted in such a way that the final arrangement is almost to the arrangement of type D, ATS anions in two layers, facing LDH with carboxyl groups. This further proves that such an arrangement is indeed the optimal one.

Looking at Table 5.6, we can compare the relative energies of the arrangements A, B, C and D for each of the three ATS concentrations. Arrangement D usually has the lowest energy confirming our previous assertion that models 1D, 2D and 3D represent the optimal arrangement of ATS anions (as well as 2A which is quite similar to 2D). The only exception seems to be model 1B which has lower energy than 1C and 1D. However, if we look at the other parameters in Table 5.6, we can see that in this model, the angle β deviated by over 3° after the MD, and that seems to have caused the basal spacing d_{003} to change to a value of 3.704 nm as opposed to the value 3.751 nm of models 1C and 1D which is in agreement with PXRD measurements. Due to this structural parameters disagreement, this model was excluded. By comparing Tables 5.5 and 5.6, we can see that the cell parameters did not change much after MD (with the exception of previously mentioned model 1D). This indicates that the models were already quite relaxed and well-optimised after the geometry optimisations.

Agreement with the PXRD experimental data can be seen in Table 5.7, which compares the final values of basal spacing d_{003} after MD with the original spacing

Model	Simulated d_{003} (nm)	Experimental d_{003} (nm)	Deviation
1B	3.704200	3.751	1.2477 %
1C	3.750950	3.751	0.0013 %
1D	3.750950	3.751	0.0013 %
2A	3.808002	3.808	0.0001 %
2B	3.805003	3.808	0.0787 %
2D	3.806244	3.808	0.0461 %
3B	3.822960	3.823	0.0010 %
3C	3.822970	3.823	0.0008 %
3D	3.822920	3.823	0.0021 %

Table 5.7: Comparison of basal spacing values of each model after final MD run with values from PXRD experiment.

from experiment. The only model which deviates by more than 0.1 % from the experimental value is 1B, mentioned above. All other models kept the values d_{003} close to the experimental one even after the final MD run.

A visual comparison of the simulated diffractogram from Materials Studio's Reflex module and an experimental diffractogram can be seen in Figure 5.8. The
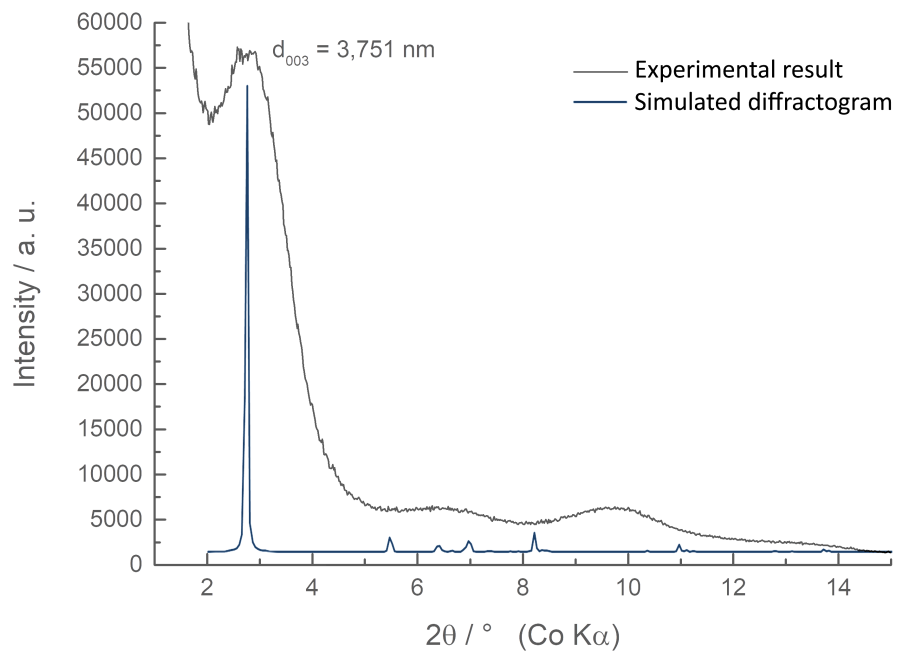
Figure 5.8: Comparison of a simulated diffractogram of model 1D after geometry optimisation with a real diffractogram of the ATS-LDH sample the simulated model was based on (figure from F. Kovanda, modified).
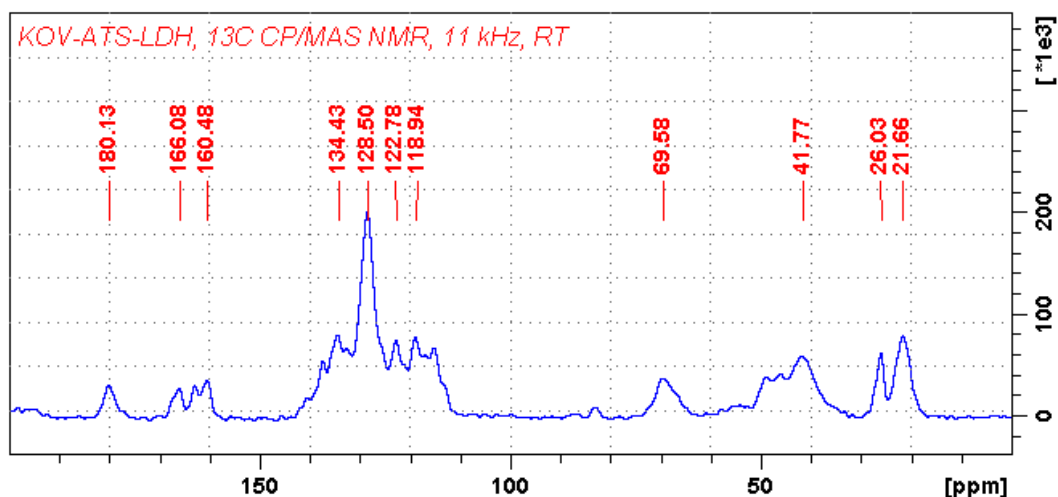
Figure 5.9: The ^{13}C MAS-NMR spectrum of the intercalated sample of ATS-LDH (figure from J. Brus).

PXRD patterns were recorded using a PANanalytical X'Pert PRO diffractometer (PANanalytical, Netherlands) with Co K$_\alpha$ radiation ($\lambda = 0.17902$ nm), with 2θ range from 0.5° to 80° 2θ with a step size of 0.2°. The HighScore 4.8 software package (PANalytical) was used for the XRD data evaluation.

The results of molecular modelling can be compared to the results of SSNMR experiments, performed by dr. Jiří Brus (Institute of Macromolecular Chemistry, Czech Academy of Sciences). Specifically ^{1}H MAS NMR, ^{13}C CP/MAS (cross-polarisation magic-angle spinning) NMR and ^{1}H-^{13}C HETCOR (heteronuclear correlation) NMR were used. The NMR spectra were measured using Bruker Avance III HD 500 WB/US NMR spectrometer (Bruker, Germany) at magic angle spinning (MAS) frequency of 11–15 kHz in 4-mm ZrO$_2$ rotors. The delay between the consecutive RF pulses was 3 s. The ^{13}C and ^{1}H NMR scales were calibrated with glycine as an external standard (176.03 ppm signal for ^{13}C; and 8.3 ppm for ^{1}H). The magic angle was set using KBr during the standard optimization procedure and the homogeneity of magnetic field was optimised using an adamantane sample.

Figure 5.9 shows the ^{13}C CP/MAS NMR spectrum of the ATS-LDH sample. The spectrum shows narrower peaks than a spectrum of atorvastatin calcium, suggesting there is some order present. This corresponds to our findings from molecular simulations, which showed a certain level of ordering of the anions in the LDH interlayer. The most significant narrowing is observed for the signals at 180 ppm which is a peak corresponding to the ATS COO$^-$ group. The detected chemical shift confirmed the dissociated, charge negative character of the terminal carboxyl group and the signal narrowing reflected the relatively uniform arrangement and regular hydrogen bonding of these units. This corresponds to
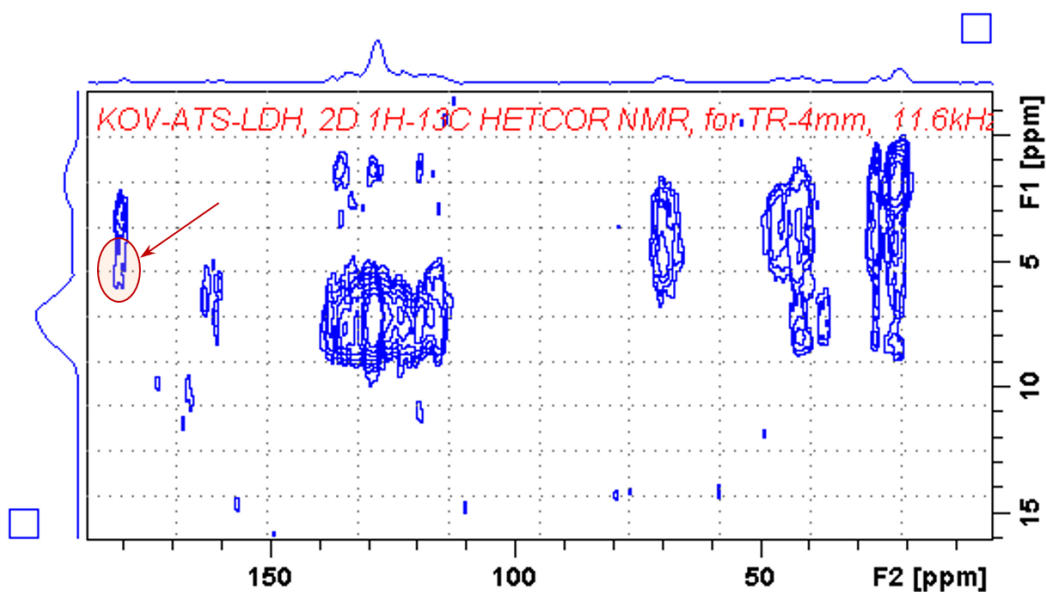
Figure 5.10: ^{1}H-^{13}C HETCOR NMR spectrum of ATS-LDH. The circle and arrow highlight the correlation peak indicating interaction between the carboxyl groups of ATS and OH groups of LDH (figure from J. Brus).

the molecular simulations' findings mentioned above. In order to identify the most prominent proton species present in the vicinity of the carboxyl groups of ATS, a series of ^{1}H-^{13}C HETCOR experiments was performed. The correlation map is shown in Figure 5.10. A medium-range correlation signal at 4-5 ppm in ^{1}H resonance frequency region can be observed. These resonances at 4.5 ppm can be attributed to the OH groups in LDH layers, indicating at least partial interactions between the ATS COO$^-$ groups and the LDH OH groups. These findings are in agreement with the hydrogen bonding observed in the simulated models (Figure 5.7).

Conclusion

Three different concentrations of atorvastatin intercalated into Mg_2Al-LDH were investigated using molecular simulations. For all concentrations, the positioning of atorvastatin molecules in two layers perpendicular to the LDH layers seems the most likely and most stable, with the carboxyl end of the molecule interacting with the hydroxyl groups of the LDH through weak non-bond interactions.

Based on the performed simulations as well as the used experimental findings, the most suitable ATS-LDH structure appears to be the one with the atorvastatin content of 75.80 %, denoted as model 2 in our simulations. Having an ATS/Al molar ratio of 1.0, it contains the maximum possible amount of atorvastatin molecules. This model with a high amount of intercalated ATS seems to be quite stable. Other models (in particular model 1, which contained the lowest amount of ATS) often exhibited clustering of atorvastatin anions close to the LDH layers, leaving gaps in the middle of the structure. Model 2, containing more anions than the other models, seemed the least prone to this.

The failure of model 2C as well as the arrangements observed in models 1C and 3C indicate that the arrangement of atorvastatin anions with carboxyl groups away from the LDH layers is unlikely to occur. This is in agreement with the NMR experimental results mentioned below which indicate an interaction between the COO^- carboxyl group of ATS and OH hydroxyl groups of LDH.

Basal spacings from PXRD experimental measurements were used as a starting point for the simulations and the models with atorvastatin molecules facing the LDH layers with their carboxyl ends maintained very similar basal spacings at the end of the simulations as well.

The interaction of atorvastatin's COO^- groups with the LDH's OH groups which was shown in our simulations as well as the partial ordering of atorvastatin anions within the layers was subsequently confirmed by NMR spectroscopic data, which showed interactions of the mentioned groups as well.

Overall, we have shown that molecular simulations are a valuable method for examining the arrangement of species intercalated into LDH and they can help determine the most likely arrangement as well as the optimal concentration and gain more insight into what is happening in the structure on a molecular level.

References

Accelrys. *Materials Studio modelling environment. Release 4.3 Documentation*. Accelrys Software Inc, San Diego, 2004.

Allured, V. S.; Kelly, C. M., and Landis, C. R. SHAPES empirical force field: new treatment of angular potentials and its application to square-planar transition-metal complexes. *Journal of the American Chemical Society*, 113(1):1–12, January 1991. doi: 10.1021/ja00001a001.

Andersen, H. C. Molecular dynamics simulations at constant pressure and/or temperature. *The Journal of Chemical Physics*, 72(4):2384–2393, February 1980. doi: 10.1063/1.439486.

Andrew, E. R.; Bradbury, A., and Eades, R. G. Nuclear magnetic resonance spectra from a crystal rotated at high speed. *Nature*, 182(4650):1659–1659, December 1958. doi: 10.1038/1821659a0.

Arai, Y. and Ogawa, M. Preparation of Co–Al layered double hydroxides by the hydrothermal urea method for controlled particle size. *Applied Clay Science*, 42(3-4):601–604, January 2009. doi: 10.1016/j.clay.2008.04.011.

Aue, W. P.; Bartholdi, E., and Ernst, R. R. Two-dimensional spectroscopy. application to nuclear magnetic resonance. *The Journal of Chemical Physics*, 64 (5):2229–2246, March 1976. doi: 10.1063/1.432450.

Barhoumi, H.; Maaref, A.; Rammah, M.; Martelet, C.; Jaffrezic, N.; Mousty, C.; Vial, S., and Forano, C. Urea biosensor based on Zn3Al–urease layered double hydroxides nanohybrid coated on insulated silicon structures. *Materials Science and Engineering: C*, 26(2-3):328–333, March 2006. doi: 10.1016/j.msec.2005. 10.042.

Bellotto, M.; Rebours, B.; Clause, O.; Lynch, J.; Bazin, D., and Elkaïm, E. A reexamination of hydrotalcite crystal chemistry. *The Journal of Physical Chemistry*, 100(20):8527–8534, January 1996. doi: 10.1021/jp960039j.

Berendsen, H. J. C.; Postma, J. P. M.; van Gunsteren, W. F.; DiNola, A., and Haak, J. R. Molecular dynamics with coupling to an external bath. *The Journal of Chemical Physics*, 81(8):3684–3690, October 1984. doi: 10.1063/1.448118.

Bergaya, F. and Lagaly, G. Chapter 1 General introduction: Clays, Clay Minerals, and Clay Science. In *Developments in Clay Science*, pages 1–18. Elsevier, 2006. doi: 10.1016/s1572-4352(05)01001-9.

Božina, N.; Ganoci, L.; Simičević, L.; Gvozdanović, K.; Domjanović, I. K.; Fistrek Prlić, M.; Križ, T.; Borić Bilušić, A.; Laganović, M., and Božina, T. Drug-drug-gene interactions as mediators of adverse drug reactions to diclofenac and statins: a case report and literature review. *Arhiv za higijenu rada i toksikologiju*, 72:114–128, June 2021. ISSN 1848-6312. doi: 10.2478/aiht-2021-72-3549.

Bragg, W. H. and Bragg, W. L. The reflection of X-rays by crystals. *Proceedings of the Royal Society of London. Series A, Containing Papers of a Mathematical and Physical Character*, 88(605):428–438, July 1913. doi: 10.1098/rspa.1913.0040.

Brooks, C. L.; Pettitt, B. M., and Karplus, M. Structural and energetic effects of truncating long ranged interactions in ionic and polar fluids. *The Journal of Chemical Physics*, 83(11):5897–5908, December 1985. doi: 10.1063/1.449621.

Broyden, C. G. *Numerical methods for unconstrained optimization*, chapter Quasi-Newton Methods, pages 87–106. Academic Press, 1972. ISBN 0125122500.

Brunauer, S.; Emmett, P. H., and Teller, E. Adsorption of gases in multimolecular layers. *Journal of the American Chemical Society*, 60(2):309–319, February 1938. doi: 10.1021/ja01269a023.

Buckingham, R. A. The classical equation of state of gaseous helium, neon and argon. *Proceedings of the Royal Society of London. Series A. Mathematical and Physical Sciences*, 168(933):264–283, oct 1938. doi: 10.1098/rspa.1938.0173.

Bullo, S.; Hussein, M. Z.; Hussein-Al-Ali, S.; Fakurazi, S., and Arulselvan, P. Antituberculosis nanodelivery system with controlled-release properties based on para-amino salicylate-zinc aluminum-layered double-hydroxide nanocomposites. *Drug Design, Development and Therapy*, page 1365, November 2013. doi: 10.2147/dddt.s50665.

Chen, C.; Gunawan, P.; Lou, X. W. D., and Xu, R. Silver nanoparticles deposited layered double hydroxide nanoporous coatings with excellent antimicrobial activities. *Advanced Functional Materials*, 22(4):780–787, December 2011. doi: 10.1002/adfm.201102333.

Chen, S.; Xu, Z. P.; Zhang, Q.; Lu, G. M.; Hao, Z. P., and Liu, S. Studies on adsorption of phenol and 4-nitrophenol on MgAl-mixed oxide derived from MgAl-layered double hydroxide. *Separation and Purification Technology*, 67 (2):194–200, June 2009. doi: 10.1016/j.seppur.2009.03.016.

Chen, X.; Shen, S.; Guo, L., and Mao, S. S. Semiconductor-based photocatalytic hydrogen generation. *Chemical Reviews*, 110(11):6503–6570, November 2010. doi: 10.1021/cr1001645.

Chibwe, K. and Jones, W. Intercalation of organic and inorganic anions into layered double hydroxides. *Journal of the Chemical Society, Chemical Communications*, (14):926, 1989. doi: 10.1039/c39890000926.

Chuang, Y. H.; Tzou, Y. M.; Wang, M. K.; Liu, C. H., and Chiang, P. N. Removal of 2-chlorophenol from aqueous solution by Mg/Al layered double hydroxide (LDH) and modified LDH. *Industrial & Engineering Chemistry Research*, 47 (11):3813–3819, May 2008. doi: 10.1021/ie071508e.

Clausius, R. XVI. on a mechanical theorem applicable to heat. *The London, Edinburgh, and Dublin Philosophical Magazine and Journal of Science*, 40(265): 122–127, August 1870. doi: 10.1080/14786447708640370.

Comba, P.; Ströhle, M., and Hambley, T. W. The directionality of d-orbitals and molecular-mechanics calculations of octahedral transition-metal compounds. *Helvetica Chimica Acta*, 78(8):2042–2047, December 1995. doi: 10.1002/hlca. 19950780812.

Comba, P.; Hambley, T. W., and Martin, B. *Molecular modeling of inorganic compounds*. Wiley-VCH, 2009. ISBN 9783527317998.

Conterosito, E.; Palin, L.; Antonioli, D.; Viterbo, D.; Mugnaioli, E.; Kolb, U.; Perioli, L.; Milanesio, M., and Gianotti, V. Structural characterisation of complex layered double hydroxides and TGA-GC-MS study on thermal response and carbonate contamination in nitrate- and organic-exchanged hydrotalcites. *Chemistry - A European Journal*, 21(42):14975–14986, August 2015. doi: 10.1002/chem.201500450.

Cornell, W. D.; Cieplak, P.; Bayly, C. I.; Gould, I. R.; Merz, K. M.; Ferguson, D. M.; Spellmeyer, D. C.; Fox, T.; Caldwell, J. W., and Kollman, P. A. A second generation force field for the simulation of proteins, nucleic acids, and organic molecules. *Journal of the American Chemical Society*, 117(19): 5179–5197, May 1995. doi: 10.1021/ja00124a002.

Cunha, V. R. R.; de Souza, R. B.; da Fonseca Martins, A. M. C. R. P.; Koh, I. H. J., and Constantino, V. R. L. Accessing the biocompatibility of layered double hydroxide by intramuscular implantation: histological and microcirculation evaluation. *Scientific Reports*, 6(1), August 2016. doi: 10.1038/srep30547.

Dauber-Osguthorpe, P.; Roberts, V. A.; Osguthorpe, D. J.; Wolff, J.; Genest, M., and Hagler, A. T. Structure and energetics of ligand binding to proteins: Escherichia coli dihydrofolate reductase-trimethoprim, a drug-receptor system. *Proteins: Structure, Function, and Genetics*, 4(1):31–47, 1988. doi: 10.1002/ prot.340040106.

De Marco, A. pH dependence of internal references. *Journal of Magnetic Resonance (1969)*, 26(3):527–528, June 1977. doi: 10.1016/0022-2364(77)90104-4.

de Roy, A.; Forano, C.; El Malki, K., and Besse, J. P. *Expanded Clays and Other Microporous Solids*, chapter Anionic Clays: Trends in Pillaring Chemistry, pages 108–169. Van Nostrand Reinhold, New York, 1992.

Debye, P. Näherungsformeln für die Zylinderfunktionen für große Werte des Arguments und unbeschränkt veränderliche Werte des Index. *Mathematische Annalen*, 67(4):535–558, December 1909. doi: 10.1007/bf01450097.

Del Hoyo, C. Layered double hydroxides and human health: An overview. *Applied Clay Science*, 36(1-3):103–121, April 2007. doi: 10.1016/j.clay.2006.06.010.

Drugs.com. Atorvastatin calcium monograph for professionals, January 2022. URL https://www.drugs.com/monograph/atorvastatin.html.

Ermer, O. Calculation of molecular properties using force fields. applications in organic chemistry. In *Bonding forces*, pages 161–211. Springer Berlin Heidelberg, 1976. doi: 10.1007/3-540-07671-9_3.

Ernst, R. R. Nuclear magnetic resonance fourier transform spectroscopy (nobel lecture). *Angewandte Chemie International Edition in English*, 31(7):805–823, jul 1992. doi: 10.1002/anie.199208053.

Etter, M. and Dinnebier, R. E. A century of powder diffraction: a brief history. *Zeitschrift für anorganische und allgemeine Chemie*, 640(15):3015–3028, December 2014. doi: 10.1002/zaac.201400526.

Evans, D. J. Computer "experiment" for nonlinear thermodynamics of Couette flow. *The Journal of Chemical Physics*, 78(6):3297–3302, March 1983. doi: 10.1063/1.445195.

Ewald, P. P. Introduction to the dynamical theory of X-ray diffraction. *Acta Crystallographica Section A: Crystal Physics, Diffraction, Theoretical and General Crystallography*, 25(1):103–108, January 1969. doi: 10.1107/s0567739469000155.

Feitknecht, W. and Gerber, M. Zur kenntnis der Doppelhydroxyde und basischen Doppelsalze III. Über Magnesium-Aluminiumdoppelhydroxyd. *Helvetica Chimica Acta*, 25(1):131–137, February 1942. doi: 10.1002/hlca.19420250115.

Ference, B. A.; Ginsberg, H. N.; Graham, I.; Ray, K. K.; Packard, C. J.; Bruckert, E.; Hegele, R. A.; Krauss, R. M.; Raal, F. J.; Schunkert, H.; Watts, G. F.; Borén, J.; Fazio, S.; Horton, J. D.; Masana, L.; Nicholls, S. J.; Nordestgaard, B. G.; van de Sluis, B.; Taskinen, M.-R.; Tokgözoğlu, L.; Landmesser, U.; Laufs, U.; Wiklund, O.; Stock, J. K.; Chapman, M. J., and Catapano, A. L. Low-density lipoproteins cause atherosclerotic cardiovascular disease. 1. Evidence from genetic, epidemiologic, and clinical studies. A consensus statement from the European Atherosclerosis Society Consensus Panel. *European Heart Journal*, 38(32):2459–2472, April 2017. doi: 10.1093/eurheartj/ehx144.

Fernon, V.; Vichot, A.; Colombet, P.; Damme, H. V., and Béguin, F. Synthesis and structure of calcium aluminate hydrates intercalated by aromatic sulfonates. *Materials Science Forum*, 152-153:335–338, March 1994. doi: 10.4028/www.scientific.net/msf.152-153.335.

Fletcher, R. Function minimization by conjugate gradients. *The Computer Journal*, 7(2):149–154, February 1964. doi: 10.1093/comjnl/7.2.149.

Gabrovska, M.; Nikolova, D.; Shopska, M.; Bilyarska, L.; Edreva-Kadjieva, R.; Crişan, D.; Stănică, N., and Crişan, M. Ni–Al layered double hydroxides as precursors of ceramic pigments. In *Proceedings of the III Advanced Ceramics and Applications Conference*, pages 205–220. Atlantis Press, November 2015. doi: 10.2991/978-94-6239-157-4_15.

Giacovazzo, C., editor. *Fundamentals of crystallography*. International Union of Crystallography, 1992. ISBN 0198555792.

González, M. Force fields and molecular dynamics simulations. *École thématique de la Société Française de la Neutronique*, 12:169–200, 2011. doi: 10.1051/sfn/201112009.

Grundy, S. M.; Stone, N. J.; Bailey, A. L.; Beam, C.; Birtcher, K. K.; Blumenthal, R. S.; Braun, L. T.; De Ferranti, S.; Faiella-Tommasino, J.; Forman, D. E., and others. 2018 AHA/ACC/AACVPR/AAPA/ABC/ACPM/ADA/AGS/APhA/ASPC/NLA/PCNA guideline on the management of blood cholesterol: a report of the american college of cardiology/american heart association task force on clinical practice guidelines. *Journal of the American College of Cardiology*, 73(24):e285–e350, 2019.

Haile, J. M. and Gupta, S. Extensions of the molecular dynamics simulation method. II. isothermal systems. *The Journal of Chemical Physics*, 79(6):3067–3076, September 1983. doi: 10.1063/1.446137.

Hestenes, M. and Stiefel, E. Methods of conjugate gradients for solving linear systems. *Journal of Research of the National Bureau of Standards*, 49(6):409, December 1952. doi: 10.6028/jres.049.044.

Hoover, W. G. Canonical dynamics: Equilibrium phase-space distributions. *Physical Review A*, 31(3):1695–1697, March 1985. doi: 10.1103/physreva.31.1695.

Hoover, W. G.; Ladd, A. J. C., and Moran, B. High-strain-rate plastic flow studied via nonequilibrium molecular dynamics. *Physical Review Letters*, 48 (26):1818–1820, June 1982. doi: 10.1103/physrevlett.48.1818.

Hünenberger, P. H. Thermostat algorithms for molecular dynamics simulations. In *Advanced Computer Simulation*, pages 105–149. Springer Berlin Heidelberg, January 2005. doi: 10.1007/b99427.

Jin, S.; Fallgren, P. H.; Morris, J. M., and Chen, Q. Removal of bacteria and viruses from waters using layered double hydroxide nanocomposites. *Science and Technology of Advanced Materials*, 8(1-2):67–70, January 2007. doi: 10.1016/j.stam.2006.09.003.

Jones, J. E. On the determination of molecular fields. —II. from the equation of state of a gas. *Proceedings of the Royal Society of London. Series A, Containing Papers of a Mathematical and Physical Character*, 106(738):463–477, October 1924. doi: 10.1098/rspa.1924.0082.

Káfuňková, E.; Taviot-Guého, C.; Bezdička, P.; Klementová, M.; Kovář, P.; Kubát, P.; Mosinger, J.; Pospíšil, M., and Lang, K. Porphyrins intercalated in Zn/Al and Mg/Al layered double hydroxides: Properties and structural arrangement. *Chemistry of Materials*, 22(8):2481–2490, March 2010. doi: 10.1021/cm903125v.

Kameda, T.; Tsuchiya, Y.; Yamazaki, T., and Yoshioka, T. Preparation of Mg–Al layered double hydroxides intercalated with alkyl sulfates and investigation of their capacity to take up N,N-dimethylaniline from aqueous solutions. *Solid State Sciences*, 11(12):2060–2064, December 2009. doi: 10.1016/j.solidstatesciences.2009.09.008.

Kane, S. P. Atorvastatin. *ClinCalc DrugStats Database*, September 2021. URL https://clincalc.com/DrugStats/Drugs/Atorvastatin.

Karvaly, G. B.; Karádi, I.; Vincze, I.; Neely, M. N.; Trojnár, E.; Prohászka, Z.; Imreh, É.; Vásárhelyi, B., and Zsáry, A. A pharmacokinetics-based approach to the monitoring of patient adherence to atorvastatin therapy. *Pharmacology Research & Perspectives*, 9(5), September 2021. doi: 10.1002/prp2.856.

Keeler, J. *Understanding NMR spectroscopy*. John Wiley and Sons, 2010. ISBN 9780470746097.

Kittel, C. *Introduction to solid state physics*. Wiley, 2005. ISBN 047141526X.

Klementová, Š.; Petráňová, P., and Fojtíková, P. Photodegradation of atorvastatin under light conditions relevant to natural waters and photoproducts toxicity assessment. *Open Journal of Applied Sciences*, 10(04):489–499, 2021. doi: 10.4236/ojapps.2021.104035.

Krivovichev, S. V.; Yakovenchuk, V. N.; Zolotarev, A. A.; Ivanyuk, G. N., and Pakhomovsky, Y. A. Cation ordering and superstructures in natural layered double hydroxides. *CHIMIA*, 64(10):730, October 2010. doi: 10.2533/chimia. 2010.730.

Kura, A. U.; Hussein, M. Z.; Fakurazi, S., and Arulselvan, P. Layered double hydroxide nanocomposite for drug delivery systems; bio-distribution, toxicity and drug activity enhancement. *Chemistry Central Journal*, 8(1), August 2014. doi: 10.1186/s13065-014-0047-2.

Kuthati, Y.; Kankala, R. K., and Lee, C.-H. Layered double hydroxide nanoparticles for biomedical applications: Current status and recent prospects. *Applied Clay Science*, 112-113:100–116, August 2015. doi: 10.1016/j.clay.2015.04.018.

Ladewig, K.; Niebert, M.; Xu, Z. P.; Gray, P. P., and Lu, G. Q. Efficient siRNA delivery to mammalian cells using layered double hydroxide nanoparticles. *Biomaterials*, 31(7):1821–1829, March 2010. doi: 10.1016/j.biomaterials.2009.10.058.

Lemons, D. S. and Gythiel, A. Paul langevin's 1908 paper "on the theory of brownian motion" ["sur la théorie du mouvement brownien," c. r. acad. sci. (paris) 146, 530–533 (1908)]. *American Journal of Physics*, 65(11):1079–1081, nov 1997. doi: 10.1119/1.18725.

Lodge, O. The influence of a magnetic field on radiation frequency. *Proceedings of the Royal Society of London*, 60(359-367):513–514, December 1897. doi: 10.1098/rspl.1896.0079.

Macedo, A. F.; Taylor, F. C.; Casas, J. P.; Adler, A.; Prieto-Merino, D., and Ebrahim, S. Unintended effects of statins from observational studies in the general population: systematic review and meta-analysis. *BMC Medicine*, 12 (1), March 2014. doi: 10.1186/1741-7015-12-51.

Mackerell, A. D. Empirical force fields for biological macromolecules: Overview and issues. *Journal of Computational Chemistry*, 25(13):1584–1604, 2004. doi: 10.1002/jcc.20082.

Mayo, S. L.; Olafson, B. D., and Goddard, W. A. DREIDING: a generic force field for molecular simulations. *The Journal of Physical Chemistry*, 94(26): 8897–8909, December 1990. doi: 10.1021/j100389a010.

Mishra, G.; Dash, B.; Sethi, D.; Pandey, S., and Mishra, B. K. Orientation of organic anions in zn-al layered double hydroxides with enhanced antibacterial property. *Environmental Engineering Science*, 34(7):516–527, July 2017. doi: 10.1089/ees.2016.0531.

Mishra, G.; Dash, B., and Pandey, S. Layered double hydroxides: A brief review from fundamentals to application as evolving biomaterials. *Applied Clay Science*, 153:172–186, March 2018. doi: 10.1016/j.clay.2017.12.021.

Mohrig, J. R.; Hammond, C. N., and Schatz, P. F. *Techniques in Organic Chemistry*. W. H. Freeman, 2006. ISBN 9780716769354.

Moore, D. M. and Reynolds Jr., C. R. *X-ray diffraction and the identification and analysis of clay minerals*. Oxford University Press, 1997. ISBN 0195087135.

Morel-Desrosiers, N.; Pisson, J.; Israëli, Y.; Taviot-Guého, C.; Besse, J.-P., and Morel, J.-P. Intercalation of dicarboxylate anions into a Zn–Al–Cl layered double hydroxide: microcalorimetric determination of the enthalpies of anion exchange. *J. Mater. Chem.*, 13(10):2582–2585, 2003. doi: 10.1039/b303953f.

Nemati, M.; Srai, M., and Rudrangi, R. Statin-induced autoimmune myopathy. *Cureus*, 13:e13576, February 2021. ISSN 2168-8184. doi: 10.7759/cureus.13576.

Nosé, S. A molecular dynamics method for simulations in the canonical ensemble. *Molecular Physics*, 52(2):255–268, June 1984a. doi: 10.1080/00268978400101201.

Nosé, S. A unified formulation of the constant temperature molecular dynamics methods. *The Journal of Chemical Physics*, 81(1):511–519, July 1984b. doi: 10.1063/1.447334.

Overhauser, A. W. Polarization of nuclei in metals. *Physical Review*, 92(2): 411–415, October 1953. doi: 10.1103/physrev.92.411.

Parrinello, M. and Rahman, A. Polymorphic transitions in single crystals: A new molecular dynamics method. *Journal of Applied Physics*, 52(12):7182–7190, December 1981. doi: 10.1063/1.328693.

Pimentel, C.; de la Luz, A. P.; Hernández-Laguna, A., and Sainz-Díaz, C. I. Effects of the cation ordering in Mg:Al and Zn:Al layered double hydroxides on crystallographic and spectroscopical properties by means of first principles calculations. *Applied Clay Science*, 223:106496, June 2022. doi: 10.1016/j.clay.2022.106496.

Polak, E. and Ribière, G. Note on the convergence of the conjugate gradient methods. *Revue Française d'Informatique et de Recherche Opérationnelle*, 3 (16):35–43, 1969.

Rappe, A. K.; Casewit, C. J.; Colwell, K. S.; Goddard, W. A., and Skiff, W. M. UFF, a full periodic table force field for molecular mechanics and molecular dynamics simulations. *Journal of the American Chemical Society*, 114(25): 10024–10035, December 1992. doi: 10.1021/ja00051a040.

Rappe, A. K. and Goddard, W. A. Charge equilibration for molecular dynamics simulations. *The Journal of Physical Chemistry*, 95(8):3358–3363, April 1991. doi: 10.1021/j100161a070.

Reif, B.; Ashbrook, S. E.; Emsley, L., and Hong, M. Solid-state NMR spectroscopy. *Nature Reviews Methods Primers*, 1(1), jan 2021. doi: 10.1038/s43586-020-00002-1.

Rietveld, H. M. A profile refinement method for nuclear and magnetic structures. *Journal of Applied Crystallography*, 2(2):65–71, June 1969. doi: 10.1107/s0021889869006558.

Rives, V., editor. *Layered Double Hydroxides: Present and Future*. Nova Science Publishers Inc., New York, 2001. ISBN 1-59033-060-9.

Rives, V.; del Arco, M., and Martín, C. Layered double hydroxides as drug carriers and for controlled release of non-steroidal antiinflammatory drugs (NSAIDs): A review. *Journal of Controlled Release*, 169(1-2):28–39, July 2013. doi: 10.1016/j.jconrel.2013.03.034.

Rives, V.; del Arco, M., and Martín, C. Intercalation of drugs in layered double hydroxides and their controlled release: A review. *Applied Clay Science*, 88-89: 239–269, February 2014. doi: 10.1016/j.clay.2013.12.002.

Roelofs, J. C. A. A.; van Bokhoven, J. A.; van Dillen, A. J.; Geus, J. W., and de Jong, K. P. The thermal decomposition of Mg-Al hydrotalcites: Effects of interlayer anions and characteristics of the final structure. *Chemistry - A European Journal*, 8(24):5571–5579, December 2002. doi: 10.1002/1521-3765(20021216)8:24⟨5571::aid-chem5571⟩3.0.co;2-r.

Schiller, U. D. Dissipative particle dynamics. a study of the methodological background. Master's thesis, University of Bielefeld, 2005.

Shabanian, M.; Hajibeygi, M., and Raeisi, A. FTIR characterization of layered double hydroxides and modified layered double hydroxides. In *Layered Double Hydroxide Polymer Nanocomposites*, pages 77–101. Elsevier, 2020. doi: 10.1016/b978-0-08-101903-0.00002-7.

Shokrolahi, F.; Latif, F.; Shokrollahi, P.; Farahmandghavi, F., and Shokrollahi, S. Engineering atorvastatin loaded Mg-Mn/LDH nanoparticles and their composite with PLGA for bone tissue applications. *International Journal of Pharmaceutics*, 606:120901, September 2021. doi: 10.1016/j.ijpharm.2021.120901.

Sideris, P. J.; Nielsen, U. G.; Gan, Z., and Grey, C. P. Mg/Al ordering in layered double hydroxides revealed by multinuclear NMR spectroscopy. *Science*, 321 (5885):113–117, July 2008. doi: 10.1126/science.1157581.

Steinberg, D. Thematic review series: The pathogenesis of atherosclerosis. An interpretive history of the cholesterol controversy: Part I. *Journal of Lipid Research*, 45(9):1583–1593, September 2004. doi: 10.1194/jlr.r400003-jlr200.

Steinberg, D. Thematic review series: The pathogenesis of atherosclerosis. An interpretive history of the cholesterol controversy, part IV: The 1984 coronary primary prevention trial ends it—almost. *Journal of Lipid Research*, 47(1): 1–14, January 2006. doi: 10.1194/jlr.r500014-jlr200.

Sugano, K.; Kansy, M.; Artursson, P.; Avdeef, A.; Bendels, S.; Di, L.; Ecker, G. F.; Faller, B.; Fischer, H.; Gerebtzoff, G.; Lennernaes, H., and Senner, F. Coexistence of passive and carrier-mediated processes in drug transport. *Nature Reviews Drug Discovery*, 9(8):597–614, August 2010. doi: 10.1038/nrd3187.

Sun, H. COMPASS: An ab initio force-field optimized for condensed-phase applications: Overview with details on alkane and benzene compounds. *The Journal of Physical Chemistry B*, 102(38):7338–7364, August 1998. doi: 10.1021/jp980939v.

Tuckerman, M. E. *Statistical mechanics.* Oxford University Press, 2010. ISBN 9780198525264.

Ureña-Amate, M. D.; Boutarbouch, N. D.; del Mar Socias-Viciana, M., and González-Pradas, E. Controlled release of nitrate from hydrotalcite modified formulations. *Applied Clay Science*, 52(4):368–373, June 2011. doi: 10.1016/j.clay.2011.03.018.

Urey, H. C. and Bradley, C. A. The vibrations of pentatonic tetrahedral molecules. *Physical Review*, 38(11):1969–1978, December 1931. doi: 10.1103/physrev.38. 1969.

Veteška, M. Molekulární simulace ve strukturní analýze. Master's thesis, Univerzita Karlova, Matematicko-fyzikální fakulta, Katedra chemické fyziky a optiky, 2009.

Vucelic, M. Cation ordering in synthetic layered double hydroxides. *Clays and Clay Minerals*, 45(6):803–813, 1997. doi: 10.1346/ccmn.1997.0450604.

Ward, N. C.; Watts, G. F., and Eckel, R. H. Statin toxicity. *Circulation Research*, 124(2):328–350, January 2019. doi: 10.1161/circresaha.118.312782.

Watson, K.; Farré, M., and Knight, N. Strategies for the removal of halides from drinking water sources, and their applicability in disinfection by-product minimisation: A critical review. *Journal of Environmental Management*, 110: 276–298, November 2012. doi: 10.1016/j.jenvman.2012.05.023.

Wells, B. A. and Chaffee, A. L. Ewald summation for molecular simulations. *Journal of Chemical Theory and Computation*, 11(8):3684–3695, August 2015. doi: 10.1021/acs.jctc.5b00093.

Woodcock, L. Isothermal molecular dynamics calculations for liquid salts. *Chemical Physics Letters*, 10(3):257–261, August 1971. doi: 10.1016/0009-2614(71) 80281-6.

Yang, Q.-Z.; Chang, Y.-Y., and Zhao, H.-Z. Preparation and antibacterial activity of lysozyme and layered double hydroxide nanocomposites. *Water Research*, 47(17):6712–6718, November 2013. doi: 10.1016/j.watres.2013.09.002.

Yang, R.; Gao, Y.; Wang, J., and Wang, Q. Layered double hydroxide (LDH) derived catalysts for simultaneous catalytic removal of soot and NOx. *Dalton Transactions*, 43(27):10317, 2014. doi: 10.1039/c3dt52896k.

Zhao, Y.; Wang, C. J.; Gao, W.; Li, B.; Wang, Q.; Zheng, L.; Wei, M.; Evans, D. G.; Duan, X., and O'Hare, D. Synthesis and antimicrobial activity of ZnTi–layered double hydroxide nanosheets. *Journal of Materials Chemistry B*, 1(43):5988, 2013. doi: 10.1039/c3tb21059f.

Zhitova, E. S.; Yakovenchuk, V. N.; Krivovichev, S. V.; Zolotarev, A. A.; Pakhomovsky, Y. A., and Ivanyuk, G. Y. Crystal chemistry of natural layered double hydroxides. 3. The crystal structure of Mg,Al-disordered quintinite-2H. *Mineralogical Magazine*, 74(5):841–848, October 2010. doi: 10.1180/minmag.2010.074.5.841.

Zong, X. and Wang, L. Ion-exchangeable semiconductor materials for visible light-induced photocatalysis. *Journal of Photochemistry and Photobiology C: Photochemistry Reviews*, 18:32–49, March 2014. doi: 10.1016/j.jphotochemrev.2013.10.001.

List of Figures

List of Tables

List of Abbreviations

2D NMR	two-dimensional nuclear magnetic resonance
ADT	automated diffraction tomography
AMBER	Assistant Model Building with Energy Refinement
ATS	atorvastatin
BET	Brunauer-Emmet-Teller
CM	centre of mass
COMPASS	Condensed-phase Optimized Molecular Potentials for Atomistic Simulation Studies
COSY	correlation spectroscopy
CP/MAS	cross-pollarisation magic-angle spinning
CVFF	Consistent Valence Force Field
DSS	sodium trimethylsilylpropanesulfonate
FF	force field
FID	free induction decay
FTIR	Fourier transform infrared spectroscopy
HETCOR	heteronuclear correlation
HMG-CoA	3-hydroxy-3-methylglutaryl co-enzyme A
HSQC	heteronuclear single-quantum correlation spectroscopy
LDH	layered double hydroxides
MAS	magic-angle spinning
MC	Monte Carlo
MD	molecular dynamics
MM	molecular mechanics
NMR	nuclear magnetic resonance
NOESY	nuclear Overhauser effect spectroscopy
PXRD	powder X-ray diffraction
QEq	charge equilibration method
RF	radiofrequency
SD	stochastic dynamics
SSNMR	solid state nuclear magnetic resonance
TEM	transmission electron spectroscopy
TGA	thermogravimetric analysis
TMS	tetramethylsilane
TMSP	trimethylsilylpropanoic acid
TOCSY	total correlation spectroscopy
UFF	Universal Force Field
XRD	X-ray diffraction